ACSNANO

www.acsnano.org

ARTICLE

Magnetic Metal–Organic Framework-Based Nanoplatform with Platelet Membrane Coating as a Synergistic Programmed Cell Death Protein 1 Inhibitor against Hepatocellular Carcinoma

Hong Guo,[‖] Yuping Liu,[‖] Xia Li, Hong Wang, Dengxuan Mao, Liangyin Wei, Xietao Ye, Ding Qu, Jiege Huo,* and Yan Chen*

Cite This: *ACS Nano* 2023, 17, 23829–23849

Read Online

ACCESS | Metrics & More | Article Recommendations | Supporting Information

ABSTRACT: Programmed cell death protein 1 (PD-1) inhibitors are the most common immune-checkpoint inhibitors and considered promising drugs for hepatocellular carcinoma (HCC). However, in clinical settings, they have a low objective response rate (15%–20%) for patients with HCC; this is because of the insufficient level and activity of tumor-infiltrating T lymphocytes (TILs). The combined administration of oxymatrine (Om) and astragaloside IV (As) can increase the levels of TILs by inhibiting the activation of cancer-associated fibroblasts (CAFs) and improve the activity of TILs by enhancing their mitochondrial function. In the present study, we constructed a magnetic metal–organic framework (MOF)-based nanoplatform with platelet membrane (Pm) coating (PmMN@Om&As) to simultaneously deliver Om and As into the HCC microenvironment. We observed that PmMN@Om&As exhibited a high total drug-loading capacity (33.77 wt %) and good immune escape. Furthermore, it can target HCC tissues in a magnetic field and exert long-lasting effects. The HCC microenvironment accelerated the disintegration of PmMN@Om&As and the release of Om&As, thereby increasing the level and activity of TILs by regulating CAFs and the mitochondrial function of TILs. In addition, the carrier could synergize with Om&As by enhancing the oxygen consumption rate and proton efflux rate of TILs, thereby upregulating the mitochondrial function of TILs. Combination therapy with PmMN@Om&As and α-PD-1 resulted in a tumor suppression rate of 84.15% and prolonged the survival time of mice. Our study provides a promising approach to improving the antitumor effect of immunotherapy in HCC.

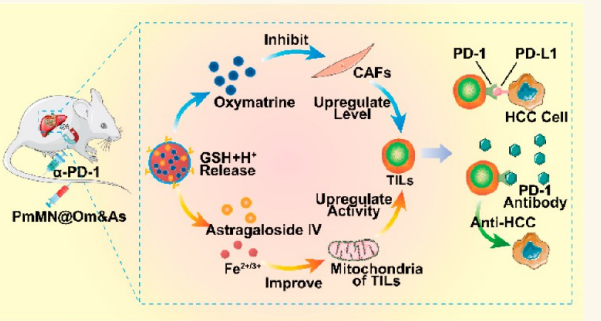

KEYWORDS: *tumor-infiltrating T lymphocytes, cancer-associated fibroblasts, mitochondria, PD-1 inhibitors, combination therapy*

Hepatocellular carcinoma (HCC) is the third leading cause of cancer-related deaths worldwide. It is considered one of the most challenging cancer types with poor prognosis.[1−3] Although surgery, radiotherapy, and chemotherapy are common curative approaches for HCC in clinical settings, their efficacy remains unsatisfactory; furthermore, they have notable side effects.[4−10] Recently, immune-checkpoint inhibitor (ICI)-based tumor immunotherapy has demonstrated promising efficacy in early phase trials;[11,12] in addition, it has exhibited superior safety in patients with HCC.[13−15] Programmed cell death protein 1 (PD-1) inhibitors, the most common ICIs, is considered a promising treatment approach for HCC.[3,16−18] PD-1 inhibitors can reactivate the antitumor function of tumor-infiltrating T lymphocytes (TILs) by inhibiting the interaction between programmed death-ligand 1 and PD-1.[19] However, in clinical settings, the objective response rate of PD-1 inhibitors is only 15%–20%.[20,21] Therefore, improving the antitumor effect of

Received: August 22, 2023
Revised: November 16, 2023
Accepted: November 17, 2023
Published: November 22, 2023

Scheme 1. Schematic Representation of the Combination Therapy against HCC by Increasing the Level and Activity of TILs Simultaneously[a]

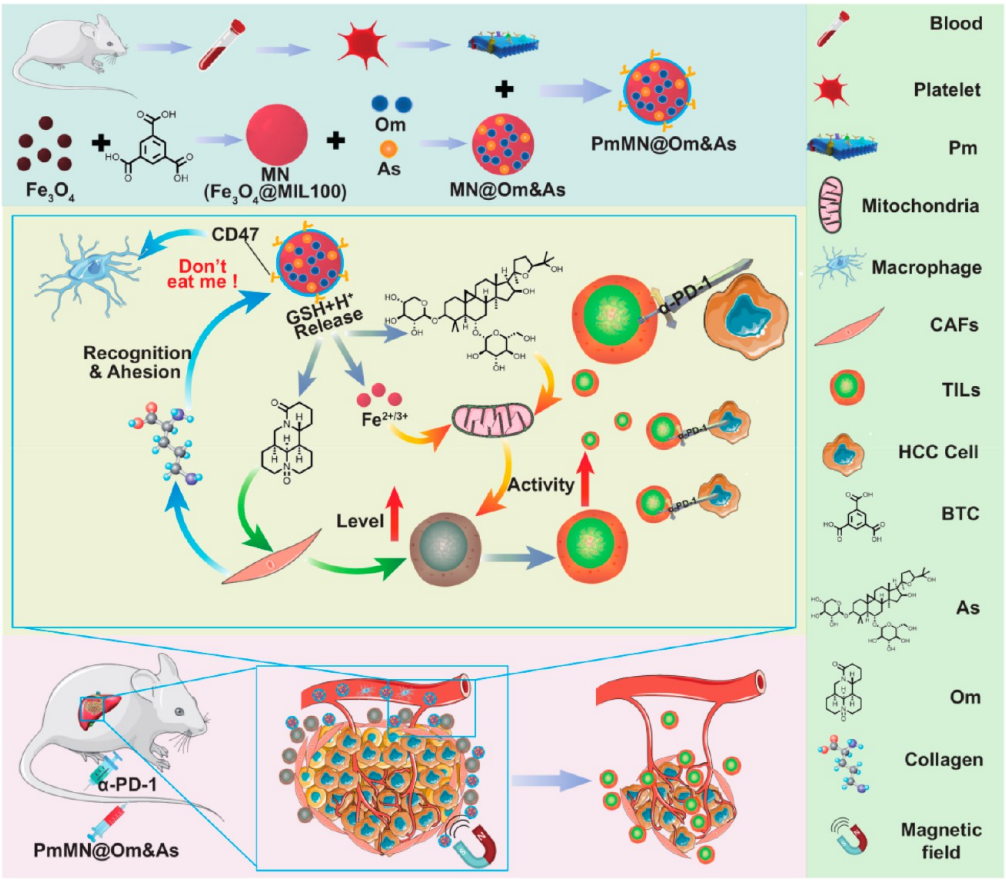

[a]MN is synthesized using Fe_3O_4 nanoparticles as precursors, followed by postloading to form MN@Om&As, and finally, Pm is modified on the surface of MN@Om&As to obtain PmMN@Om&As. PmMN@Om&As evade clearance by the MPS through surface CD47 and target HCC tissue under external magnetic field guidance combined with the specific recognition and adhesion of Pm to collagen. In the reductive and acidic HCC microenvironment, Om and As are accelerated release from PmMN@Om&As. Then, Om plays a role in enhancing tumor infiltration of TILs by inhibiting CAF activation, while As synergistically improves the mitochondrial function of TILs with the of $Fe^{2+/3+}$ from the carrier, ultimately enhancing their activity. The combined application of α-PD-1 further contributes to the antitumor effects.

PD-1 inhibitors is an urgent but challenging task for HCC treatment.[22,23]

The level of TILs is a crucial factor that influences the efficacy of PD-1 inhibitors.[19] In the HCC microenvironment, cancer-associated fibroblasts (CAFs) construct a mesenchymal barrier by secreting collagen, fibroblast activation protein (FAP), and C-X-C motif chemokine ligand 12 (CXCL12) to suppress the intratumoral infiltration of TILs;[24−26] this can reduce the level of TILs. Oxymatrine (Om) is a soluble alkaloid in Sophorae flavescentis radix, and it could inhibit CAF activation by reversing epithelial−mesenchymal transition in our previous study.[27] Therefore, inhibiting the activation of CAF by Om can raise the level of TILs. Nevertheless, TILs themselves still exhibit insufficient activity. According to the report of Ho et al., HCC microenvironment-induced metabolic stress impairs the functions of the mitochondria in TILs; this mitochondrial dysfunction decreases ATP production, further attenuating the antitumor activity of TILs.[28−30] Astragaloside IV (As) is an insoluble tetracyclic triterpenoid in Astragali Radix that can improve the mitochondrial function of TILs by upregulating the expression of peroxisome proliferator-activated receptor-γ coactivator-1α (PGC-1α).[31] Improving the mitochondrial function of TILs by As is an effective strategy to enhance the activity of TILs. Therefore, the combined administration of Om and As may be a promising strategy to simultaneously increase the levels and activities of TILs. However, this strategy has limited pharmaceutical applications owing to the poor bioavailability and biodistribution of Om and As, making it difficult to deliver these agents to HCC tissues.

Metal−organic frameworks (MOFs) are a class of organic−inorganic porous materials constructed using metal centers and organic linkers, which may improve drug bioavailability and biodistribution.[32−34] The different polarities of Om and As make it significantly challenging for normal nanosystems to coload them with a high drug-loading capacity (DLC). Interestingly, MOFs have a highly adaptive internal environment for loading drugs with different polarities.[35−37] The large surface area and pore volume of MOFs facilitate the loading of Om and As with a high DLC. Moreover, the Fe_3O_4@MIL100 MOF is constructed using magnetic Fe_3O_4 as a metal center; this MOF can target HCC tissues in a magnetic field.[38]

In vivo, the mononuclear phagocyte system (MPS) is a barrier for drug delivery that can capture and remove nanoparticles. Now, platelet membrane (Pm) coating has been an effective technique for evading clearance by the MPS.

https://doi.org/10.1021/acsnano.3c07885
ACS Nano 2023, 17, 23829−23849

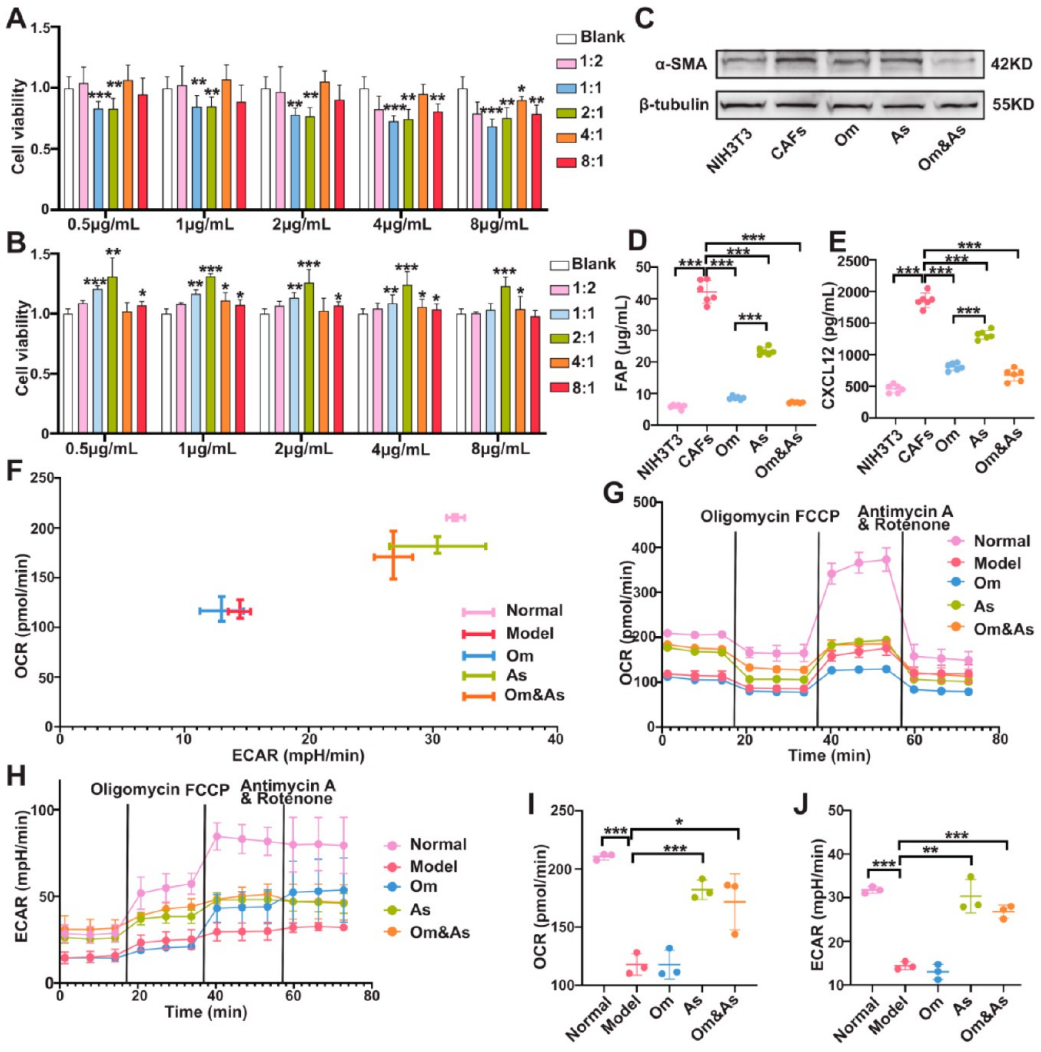

Figure 1. Inhibition of CAFs and improvement of TIL mitochondrial functions by Om&As. The effects of different ratios and concentrations of Om&As on the viability of CAFs (A) and TILs (B) were measured by CCK8 assay *in vitro* (n = 6) (vs blank). The effect of Om and As on α-SMA expression was measured by WB (C). The effect of Om and As on the ability of CAFs to secrete FAP (D) and CXCL12 was measured by ELISA (E). Role of Om and As in the mitochondrial respiration of TILs (F) (n = 3). The OCR (G) and ECAR (H) of TILs were measured using the Seahorse XF^{e}96 analyzer (n = 3), and the OCR (I) and ECAR (J) of TILs were calculated (n = 3). Data are represented as means ± SD *p < 0.05, **p < 0.01, ***p < 0.001, two-tailed Student's t test.

Pm coating can specifically recognize and adhere to CAF-secreted collagen in the HCC microenvironment, thereby generating a dual-targeting effect in synergy with magnetic fields.[39−41] Therefore, the magnetic Fe_3O_4@MIL100 MOF nanoplatform with Pm coating (PmMN) is an attractive drug delivery carrier for the simultaneous delivery of Om and As because of its structural characteristics, targeting abilities, and immune escape ability.

Our results suggest that PmMN@Om&As can deliver Om and As to the HCC microenvironment via dual-targeting mediated by magnetic fields and Pm coating; then the structure of PmMN@Om&As disintegrates in a reductive and acidic tumor microenvironment; as a result, Om&As is released to regulate the level and activity of TILs. We assessed the infiltration of TILs using flow cytometry; in addition, we isolated TILs from HCC tissues via magnetic-activated cell sorting (MACS) and investigated the mitochondrial function of TILs using a seahorse system. PmMN@Om&As enhanced the level and activity of TILs by inhibiting the activation of CAFs and improving the mitochondrial function of TILs, respectively. The combination of PmMN@Om&As and α-PD-1 effectively improved anti-HCC efficacy, achieving a tumor suppression rate (TSR) of 84.15% and prolonging the survival time of HCC-bearing mice. Furthermore, combination therapy decreased the volume of ascites and improved the quality of life (QOL) of mice. Based on a single mechanism, many existing strategies, including turning the "cold" tumor into a "hot" tumor,[42] improving tumor immunogenicity,[43] and reversing TIL exhaustion,[44] have been formulated to improve the efficacy of PD-1 inhibitors. However, these strategies exhibit limited effectiveness owing to the intricate nature of the tumor microenvironment. In this study, we simultaneously tackled this issue from two distinct perspectives: augmenting the level of TILs by inhibiting CAF activation and enhancing the activity of TILs by improving their mitochondrial function (Scheme 1). As a result, we provided an efficient drug delivery system with promising potential in the clinical immunotherapy of HCC.

https://doi.org/10.1021/acsnano.3c07885
ACS Nano 2023, 17, 23829−23849

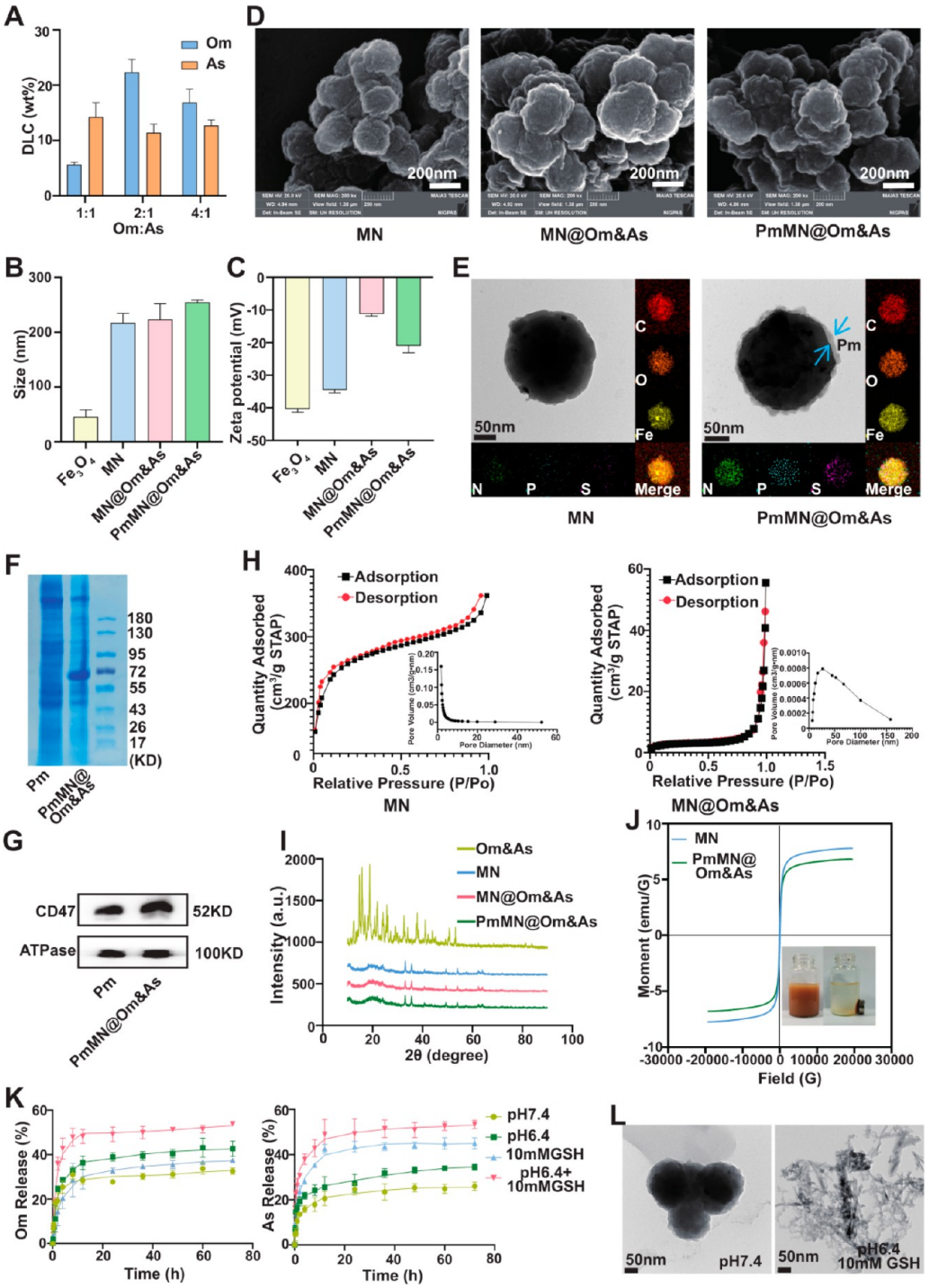

Figure 2. Characterization of PmMN@Om&As. The DLC of PmMN@Om&As was changed by adjusting the Om and As concentration ratio in the drug-loading system (A). The size distribution (B) and zeta potential (C) of Fe_3O_4, MN, MN@Om&As, and PmMN@Om&As were determined by isomorphic DLS (n = 3). Images showing the morphology of MN, MN@Om&As, and PmMN@Om&As were obtained using SEM (scale bar = 200 nm) (D). Images showing the morphology and elements of MN and PmMN@Om&As were obtained using TEM (scale bar = 50 nm) (E). The protein profile of PmMN@Om&As was obtained using SDS-PAGE (F). CD47 of the PmMN@Om&As was observed by WB (G). The pore characteristics of MN and MN@Om&As were observed by the curves of nitrogen adsorption and desorption (H). The crystal structure of the sample was observed by XRD (I). The responsiveness of PmMN@Om&As to magnetic fields was tested by VSM and NdFeB permanent magnets (J). Effects of reductive and acidic environment on drug release of PmMN@Om&As (n = 3) (K). TEM images showed the effects of reductive and acidic environments on PmMN@Om&As (L). Data are presented as means ± SD.

RESULTS AND DISCUSSION

Inhibition of CAF Activity and Enhancement of TIL Mitochondrial Functions by Om&As. An optimal mass ratio is important for Om&As to inhibit CAF activation and enhance TIL mitochondrial functions simultaneously; thus, we induced NIH3T3 cells to differentiate into CAFs using transforming growth factor-β1[27,45] and simulated an *in vitro* TIL model by coculturing CTLL-2 cells with H22 cells.[46] The

https://doi.org/10.1021/acsnano.3c07885
ACS Nano 2023, 17, 23829−23849

effect of different mass ratios (1:2−8:1) of Om&As on CAF and TIL activities was observed. The results indicated that the desired efficacy was observed at a mass ratio of 2:1, manifesting the inhibition of CAF activity and enhancing the activity of TILs simultaneously (Figure 1A, B).

A high level of α-smooth muscle actin (α-SMA) is a characteristic of CAFs.[47] In the present study, Western blotting (WB) showed that both Om and Om&As markedly decreased α-SMA levels (Figure 1C), suggesting that they effectively inhibited CAF activation. FAP and CXCL12 secreted by CAFs suppressed TIL infiltration into the tumor microenvironment. Enzyme-linked immunosorbent assay (ELISA) results showed that the secretion of FAP and CXCL12 in the Om and Om&As groups was significantly lower than that in the CAF group (Figure 1D, E), indicating that Om&As effectively suppressed FAP and CXCL12 secretion by CAFs.

Seahorse analysis is a valuable method to assess the respiratory status of mitochondria in TILs. It could assess mitochondrial aerobic and anaerobic respiratory functions by measuring the oxygen consumption rate (OCR) and extracellular acidification rate (ECAR), respectively.[29] No significant difference was observed in the ECAR or OCR between the Om and model groups. However, in the As group, OCR was 2.11 times higher ($p < 0.001$) and ECAR was 1.56 times higher ($p < 0.01$) than those of the model group. Similarly, in the Om&As group, OCR was 1.86 times higher ($p < 0.05$) and ECAR was 1.45 times higher ($p < 0.001$) than those of the model group (Figure 1F−J). Furthermore, improved basal respiration, maximum respiration, and ATP production were observed in TILs in the As and Om&As groups (Figure 1G), which suggested that As and Om&As improved aerobic and anaerobic respiration in TILs.

Overall, these results confirmed that Om&As (2:1) inhibited the activation of CAFs and improved the mitochondrial function of TILs *in vitro*. This indicates the potential of Om and As to enhance the level and activity of TILs.

Fabrication and Characterization of PmMN@Om&As. Fe_3O_4@MIL100 magnetic MOF has been extensively studied for protein adsorption and magnetic recyclability. However, its application in codelivering drugs remains unexplored. In the present study, we discovered their excellent potential for the simultaneous loading of drugs with different polarities.

Initially, Fe_3O_4 nanoparticles were synthesized using a solvothermal method according to the Shao et al. study.[48] Next, Fe_3O_4@MIL100 magnetic MOF nanoplatform (MN) was synthesized using the Fe_3O_4 nanoparticles as a precursor according to a previously reported procedure.[49−52] Subsequently, MN@Om&As was obtained by postloading using the MN as a precursor. Finally, the Pm was modified on the surface of the MN@Om&As by sonicating to obtain PmMN@Om&As.[53,54]

To achieve the mass ratio of 2:1 between Om and As in PmMN@Om&As, Om&As solutions with different concentration ratios were selected for drug loading. When the concentration ratio between Om and As in the Om&As solution was 2:1, the mass ratio between Om and As in PmMN@Om&As was approximately 2:1. The DLC values of Om and As were 22.37 and 11.40 wt %, whereas the total DLC was 33.77 wt % (Figure 2A).

The results of dynamic light scattering (DLS) showed that the size of PmMN@Om&As was 252.7 ± 3.2 nm (Figure 2B, Figure S1A), which was consistent with the results of scanning electron microscopy (SEM) and transmission electron microscopy (TEM) (Figure 2D, E). The size of the nanoplatform increased as the synthesis progressed: 45.72 ± 12.62 nm (Fe_3O_4 nanoparticles), 217.33 ± 17.05 nm (MN), 223.70 ± 23.00 nm (MN@Om&As), and 252.7 ± 3.2 nm (PmMN@Om&As) (Figure 2B), and the zeta potential of the nanoplatform also changed during this process: −40.37 ± 0.95 mV (Fe_3O_4 nanoparticles), −34.57 ± 0.85 mV (MN), −11.23 ± 0.61 mV (MN@Om&As), and −21.03 ± 2.06 mV (PmMN@Om&As) (Figure 2 C, Figure S1B). These changes in the size and zeta potential validated the successful completion of each synthesis step.

The SEM results showed that the MN was spherical in shape with an irregular surface (Figure 2D), which was consistent with the results reported by Wang et al.,[55] as well as the shapes of MN@Om&As and PmMN@Om&As were similar to that of the MN. The TEM results showed a Pm coating on the PmMN@Om&As surface (Figure 2E). Sodium dodecyl sulfate−polyacrylamide gel electrophoresis and WB also showed that PmMN@Om&As retained the proteins of the Pm (Figure 2F), especially CD47 (Figure 2G), which could prevent PmMN@Om&As from being cleared by the MPS.

The high DLC was attributed to the high surface area and large pore volume of the MN. Thus, we further determined surface area and pore volume by performing nitrogen adsorption−desorption experiments and calculated the corresponding parameters by the Brunauer−Emmett−Teller (BET) specific surface area detection method and Barret−Joyner−Halenda (BJH) pore volume detection method (Figure 2H). The surface area and pore volume of the MN were 832.31 m^2/g and 0.27 cm^3/g, respectively, which aligned with the theoretical estimation. However, after drug loading (MN@Om&As), the surface area and pore volume significantly decreased to 10.49 m^2/g and 0.08 cm^3/g, respectively. This reduction was attributed to pore space occupancy by Om&As. The TEM results showed that the nitrogen element content in PmMN@Om&As was more than MN, which was attributed to the presence of Om and Pm (Figure 2B, Figure S1 C, Table S1). Moreover, sulfur and phosphorus element were observed in PmMN@Om&As, which were characteristic element of Pm (Figure 2B, Figure S1 C, Table S1). The X-ray diffraction results of PmMN@Om&As did not show characteristic peaks for Om&As, which indicated that Om&As in PmMN@Om&As was amorphous in nature (Figure 2I).

During MN synthesis, the Fe_3O_4 nanoparticles produced $Fe^{2+/3+}$ ions in an acidic environment and formed an MN by a coordination reaction with 1,3,5-benzenetricarboxylic acid (BTC).[56] The remaining Fe_3O_4 nanoparticles were attached to the MN structure, which responded to magnetic fields. We tested the magnetic response abilities of the MN and PmMN@Om&As using a vibrating sample magnetometer (VSM). The results showed that the MN and PmMN@Om&As responded to magnetic fields; thus, they can be used for magnetically targeted drug delivery (Figure 2J, Figure S2D, E).

The results of drug release showed that the reductive and acidic HCC microenvironment simulated *in vitro* accelerated Om and As release from PmMN@Om&As: 30.59% of Om and 26.85% of As were released in the environment with pH 7.4, whereas 52.32% of Om and 51.38% of As were released in the reductive and acidic environment (pH6.4 + 10 mM GSH) after 72 h (Figure 2K). The TEM and DLS results showed that the PmMN@Om&As was considerably destroyed under the reductive and acidic environment (Figure 2L; Figure S1H), which was consistent with the results reported by Wang et al.[55]

https://doi.org/10.1021/acsnano.3c07885
ACS Nano 2023, 17, 23829−23849

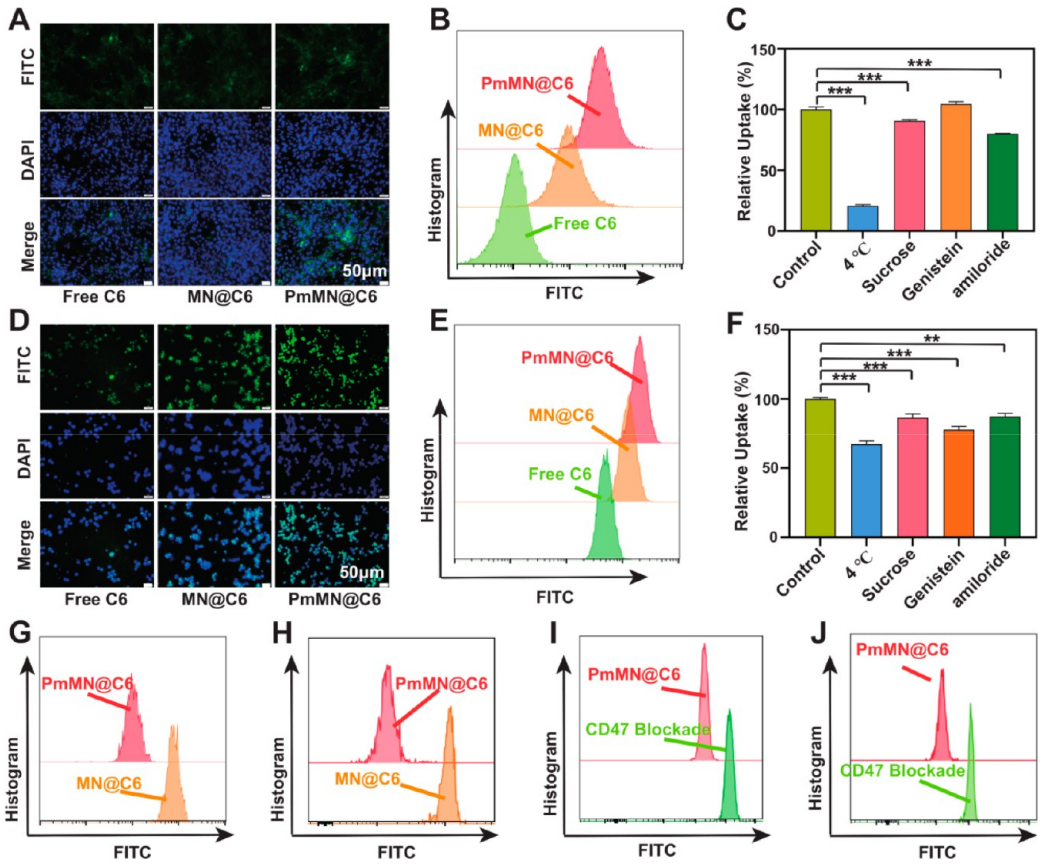

Figure 3. Cellular uptake and immune escape of PmMN@Om&As. The uptakes of free C6, MN@C6, and PmMN@C6 by CAFs were shown by fluorescence microscopy (A) (scale bar = 50 μm) and flow cytometry (B). The uptake mechanisms of PmMN@C6 by CAFs were shown by competitive inhibition assay (n = 3) (C). The uptakes of free C6, MN@C6, and PmMN@C6 by TILs were shown by fluorescence microscopy (D) (scale bar = 50 μm) and flow cytometry (E). The uptake mechanisms of PmMN@C6 by TILs were shown by competitive inhibition assay (n = 3) (F). The abilities of PmMN@Om&As to escape macrophage phagocytosis *in vitro* (G) and *in vivo* (H) were shown by flow cytometry. The abilities of PmMN@Om&As to escape macrophage phagocytosis *in vitro* (I) and *in vivo* (J) were inhibited by blocking CD47. Data are represented as the means ± SD *p < 0.05, **p < 0.01, ***p < 0.001, two-tailed Student's t test.

and Cun et al.[57] This was because the coordination bond was the main chemical bond among the Fe_3O_4@MIL100 magnetic MOF, which exhibited weak stability and was susceptible to degradation in a reductive and acidic environment.

These results indicate that we successfully prepared a magnetic MN with a Pm coating to coload Om&As. The platform accelerated Om and As release in response to an HCC microenvironment, thereby enhancing drug efficacy.

Cellular Uptake and Immune Escape of PmMN@Om&As. To investigate the uptake of PmMN@Om&As by CAFs and TILs, we selected coumarin 6 (C6) instead of Om&As.[58] The results of fluorescent microscopy and flow cytometry showed that the uptake rate of PmMN@C6 by CAFs was 37.01 (p < 0.001) and 4.02-fold (p < 0.001) higher than that of free C6 and MN@C6, respectively (Figure 3A, B; Figure S2A). Similarly, the uptake rate of PmMN@C6 by TILs was 3.89 (p < 0.001) and 1.57-fold (p < 0.001) higher than that of free C6 and MN@C6, respectively (Figure 3D, E; Figure S2B). These results suggested that PmMN@Om&As accelerated the uptake of Om&As by CAFs and TILs. Further, the underlying uptake mechanism was elucidated by performing a competitive inhibition experiment.[59] Energy-dependent endocytosis was inhibited at 4 °C, and sucrose, genistein, and amiloride were used to inhibit the clathrin- and caveolae-mediated endocytosis pathway and pinocytosis, respectively. The results indicate that CAFs and TILs endocytosed PmMN@C6 via an energy-dependent pathway (Figure 3C, F). Moreover, CAFs endocytosed PmMN@C6 via the clathrin-mediated endocytosis pathway and pinocytosis, whereas TILs endocytosed PmMN@C6 via the clathrin- and caveolae-mediated endocytosis pathway and pinocytosis (Figure 3C, F). Additionally, the presence of the Pm enhanced the uptake of PmMN@C6 by H22 cells (Figure S2C–F), which was attributed to the high affinity between the Pm coating and the cells.

RAW264.7 cells were used to explore the immune escape of PmMN@Om&As *in vitro*, and the flow cytometry results showed that the clearance rate of PmMN@C6 by RAW264.7 cells *in vitro* was only 13.58% (p < 0.001) of that of MN@C6 (Figure 3G, Figure S2G). Subsequently, our *in vivo* investigations on the immune escape behavior of PmMN@Om&As using C57BL/6 mice showed results that were consistent with the *in vitro* findings (Figure 3H, Figure S2H), which suggested that PmMN@Om&As evaded MPS clearance. CD47 is a protein expressed on Pm[60] and is a "don't eat me" signal that ligates with the signal regulatory protein α of macrophages to escape immune clearance.[61,62] Because CD47 was present on the PmMN@Om&As surface existed CD47, the protein was blocked using an anti-CD47 antibody to investigate the immune escape mechanism of PmMN@

https://doi.org/10.1021/acsnano.3c07885
ACS Nano 2023, 17, 23829–23849

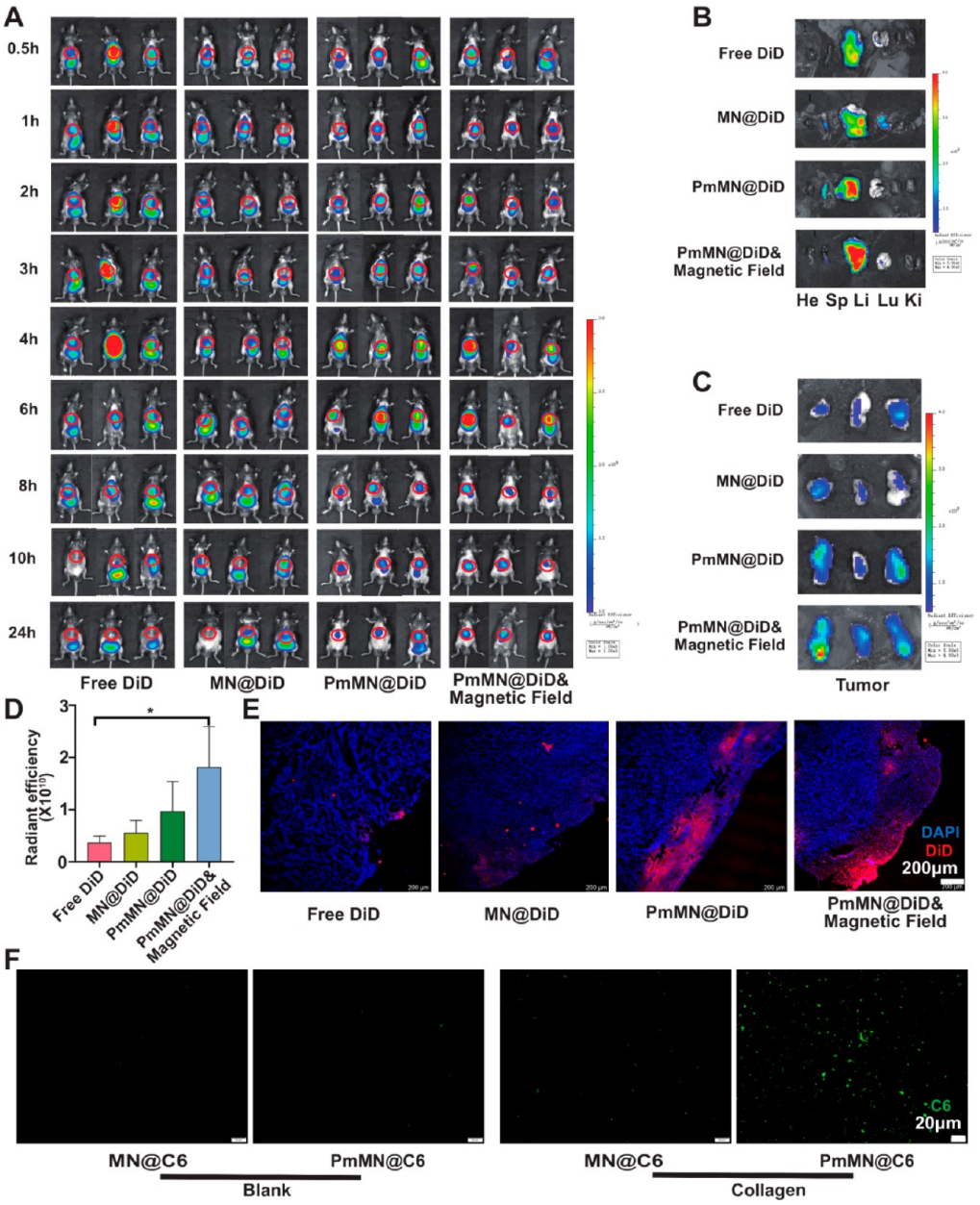

Figure 4. Biodistribution of PmMN@Om&As. The distribution of free DiD, MN@DiD, PmMN@DiD, PmMN@DiD, and magnetic field in HCC mice were visualized by IVIS Spectrum (A). After 24 h, the *ex vivo* imaging of various organs (B) and tumor tissues (C) was observed by the IVIS Spectrum. The *ex vivo* imaging of tumor tissue was analyzed (D) (n = 3). The distribution of free DiD, MN@DiD, PmMN@DiD, PmMN@DiD, and magnetic field in tumor tissue was observed by confocal laser microscopy (scale bar = 200 μm) (E). The adhesion ability of collagen to PmMN@Om&As was shown by fluorescence microscopy (scale bar = 20 μm) (F). Data are represented as the means ± SD *p < 0.05, two-tailed Student's t test.

Om&As. After blocking CD47, the *in vitro* clearance rate of PmMN@C6 by RAW264.7 cells increased markedly (Figure 3I, Figure S2I). The results substantiated that CD47 played a key role in enabling PmMN@Om&As to escape immune clearance, and this correlation was further corroborated by *in vivo* experiments (Figure 3J, Figure S2J). Additionally, the uptake rates of PmMN@C6 in CAFs and TILs did not change after blocking CD47 (Figure S2K–N), suggesting that CD47 of PmMN@Om&As would not substantially reduce Om&As uptake by CAFs and TILs, which was crucial to ensure the efficacy of PmMN@Om&As.

Overall, the present findings indicate that PmMN@Om&As enhanced cellular uptake and escaped immune clearance, thereby improving the bioavailability of Om&As. Notably, the CD47-mediated immune escape did not reduce the endocytosis efficiency of PmMN@Om&As in CAFs and TILs, which indicate that the immune escape of PmMN@Om&As would not decrease the efficacy of Om&As.

Biodistribution of PmMN@Om&As. To investigate the *in vivo* biodistribution of PmMN@Om&As, we established an orthotopic HCC model in C57BL/6 mice. For labeling, DiD was utilized as a fluorescent probe for both PmMN (PmMN@DiD) and MN (MN@DiD). Subsequently, free DiD, MN@DiD, and PmMN@DiD were administered via the tail vein to the HCC-bearing mice. To guide PmMN@DiD to the HCC tissue, an NdFeB permanent magnet was employed.

https://doi.org/10.1021/acsnano.3c07885
ACS Nano 2023, 17, 23829–23849

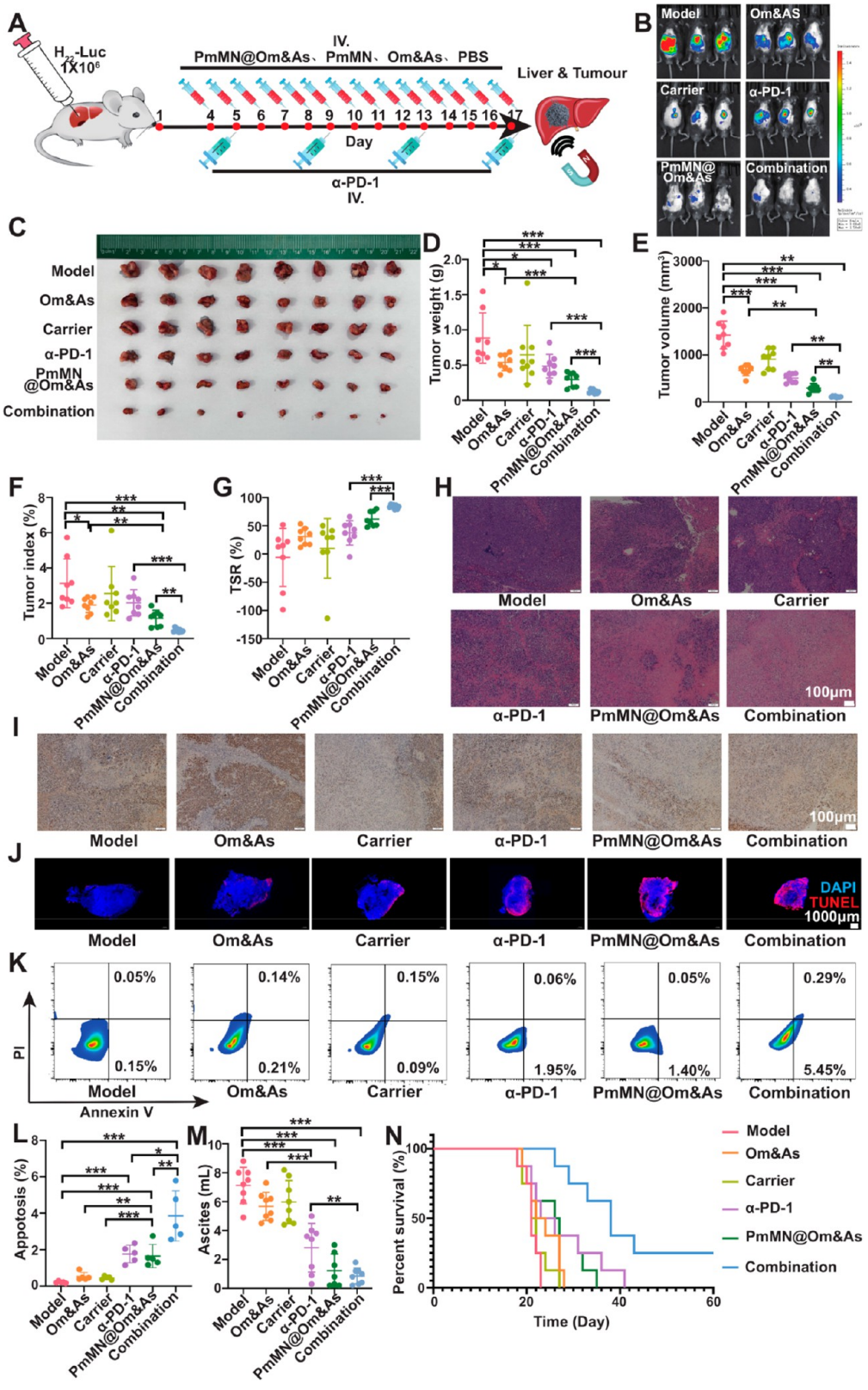

Figure 5. Synergistic antitumor effect of PmMN@Om&As and PD-1 antibody (α-PD-1) on orthotopic implant model of HCC. HCC mice were treated by the procedure shown in panel A. Tumor activity was shown by bioluminescent technology *in vivo* (B). The tumors of each group of mice are shown (C). The tumor weight (D), tumor volume (E), tumor index (F) of mice, and TSR (G) of drugs were mathematically analyzed (n = 8). The pathological structure and proliferative capacity of tumor tissues are shown by HE (H) and Ki67 (I) staining (scale bar = 100 μm). Apoptosis of tumor cells was shown by Tunel staining (J) (scale bar = 1000 μm) and flow cytometry (n = 5) (K, L). The volumes of ascites were measured and counted (n = 8) (M). The survival of mice in each group was monitored daily (n = 8) (N). Data are represented as the means ± SD *p < 0.05, **p < 0.01, ***p < 0.001, two-tailed Student's t test.

https://doi.org/10.1021/acsnano.3c07885
ACS Nano 2023, 17, 23829−23849

The *in vivo* imaging results revealed a gradual concentration of fluorescent signals in the liver region with PmMN@DiD, which was further enhanced by the presence of a magnetic field (Figure 4A). Conversely, mice treated with free DiD and MN@DiD showed widespread fluorescence signals throughout the ventral regions (Figure 4A). In comparison to the free DiD group, the mean fluorescence intensity of tumors in the PmMN@DiD & magnetic field group increased by 4.90-fold ($p < 0.05$) at 24 h postadministration (Figure 4B−D). These results suggested that PmMN@Om&As under the guidance of magnetic fields could efficiently deliver Om&As into HCC tissues.

Ex vivo imaging of excised major organs demonstrated that only the liver exhibited a strong fluorescent signal in the PmMN@DiD & magnetic field group, whereas minimal fluorescent signals were detected in other organs. In contrast, the spleen in the PmMN@DiD group and the lung and spleen in the MN@DiD group displayed detectable fluorescent signals (Figure 4B), indicating that the combination of PmMN@DiD and magnetic fields restricted the distribution of Om&As in nontarget tissues. Furthermore, after separating tumor tissue from the liver, the tumor tissues from the PmMN@DiD group and the PmMN@DiD & magnetic field group exhibited stronger fluorescent signals compared to free DiD and MN@DiD (Figure 4C, E), which suggested that the Pm coating facilitated effective targeting and prolonged retention of nanoplatforms within HCC. It is well-known that HCC tissue contains an abundance of collagen,[63,64] and collagen can serve as an agent for platelet aggregation.[65,66] We hypothesized that the PmMN@Om&As might target and adhere to HCC tissue through the recognition of Pm coating to collagen. We substantiated this hypothesis through a simulated blood perfusion experiment. The results indicated that PmMN@C6 exhibited greater adhesion to collagen-coated glass plates compared to MN@C6, whereas PmMN@C6 did not adhere to glass plates lacking collagen (Figure 4F). Recent scholarly consensus asserts that collagen secreted by CAFs can create a barrier against nanoparticle entry into the tumor microenvironment;[67−69] however, Pm coating appeared to transform collagen from an obstacle into an ally.

The preceding findings clearly demonstrate the enhanced efficacy of PmMN@Om&As when guided by magnetic fields in terms of improving the targeting and retention of Om&As within HCC tissue. The dual targeting of PmMN@Om&As toward HCC was achieved via the responsive behavior of Fe_3O_4@MIL100 magnetic MOF to the magnetic field, as well as the specific recognition of the Pm coating to collagen within the HCC microenvironment. The application of the magnetic field not only accelerated the targeting process but also increased the precision of targeting by minimizing the distribution of PmMN@Om&As in nonlesion sites such as the spleen and lungs. Furthermore, the Pm coating endowed PmMN@Om&As with both targeted delivery and sustained effects, as substantiated by its ability to enhance cellular uptake and evade immune clearance, as discussed in the preceding section. In the current landscape of nanodrug delivery system research, cell membrane coating has emerged as a prominent area of interest. Among various types of cell membranes, the Pm stands out as an ideal candidate for this study due to its capacity to simultaneously fulfill the aforementioned four crucial roles.

Synergistic Antitumor Effects of PmMN@Om&As& PD-1 Antibody (α-PD-1) in an HCC Orthotopic Implant Model.

Having established the capacity of Om&As to modulate CAF activation and improve mitochondrial function in TILs *in vitro*, and subsequently constructing PmMN@Om&As for the codelivery of Om&As within the HCC microenvironment, we proceeded to assess the anti-HCC potential of combined therapy involving PmMN@Om&As and α-PD-1 in an orthotopic HCC mouse model implanted with H22-Luc cells. Following the dosage regimen outlined in Figure 5A, various treatments including phosphate buffered saline, Om&As, blank carrier (PmMN), α-PD-1, PmMN@Om&As, or PmMN@Om&As + α-PD-1 were administered via the tail vein to the mice. An NdFeB permanent magnet was positioned over the liver area at 1 h postadministration to facilitate targeted drug delivery to the HCC site.

The tumor was monitored by using *in vivo* bioluminescence imaging, revealing that the combination therapy group exhibited the lowest bioluminescence intensity. This observation suggested that the concurrent application of PmMN@Om&As and α-PD-1 effectively inhibited tumor growth *in vivo* (Figure 5B, Figure S3). The tumors are depicted in Figure 5C, and the tumor weight and tumor volume of the combination group were 3.94-fold ($p < 0.001$) and 4.69-fold ($p < 0.01$) lower than the α-PD-1 group (Figure 5D, E). The tumor index, an indicative parameter, was notably reduced by PmMN@Om&As, as demonstrated by a statistically significant decrease. Furthermore, the combination group displayed a significant reduction in tumor index when compared to both the α-PD-1 group and the PmMN@Om&As group (Figure 5F). Meanwhile, the TSR in the combination group reached 84.15%, significantly higher than that of the α-PD-1 and PmMN@Om&As groups (Figure 5G). The above data indicate the synergistic potential of PmMN@Om&As in enhancing the therapeutic effect of α-PD-1. Moreover, it was observed that PmMN@Om&As exhibited superior anti-HCC effects compared to Om&As alone, which could be attributed to the improved biodistribution facilitated by PmMN@Om&As (Figure 5D-F). Besides, the blank carrier effectively attenuated HCC bioluminescence; however, this effect did not translate into a reduced tumor weight, volume, or tumor index (Figure 5D−F). This phenomenon might be attributed to bioluminescence relying on the Mg element in tissues, which is more reactive than Fe. Consequently, Mg replaced Fe binding to the BTC of the carrier, resulting in diminished bioluminescence.[70]

Histopathological examinations through hematoxylin and eosin (HE) staining revealed the most pronounced tumor tissue necrosis in the combination therapy group, whereas results from Ki67 staining indicate the lowest tumor tissue proliferation in the same group (Figure 5H, K). TUNEL assays and flow cytometry data further substantiated these findings by demonstrating that while both α-PD-1 and PmMN@Om&As increased tumor apoptosis rates, the combination group exhibited a significantly higher tumor apoptosis rate in comparison to both the α-PD-1 and PmMN@Om&As groups (Figure 5J−L), which implied that PmMN@Om&As potentiated the apoptotic induction ability of α-PD-1 toward HCC cells.

Ascites, a crucial indicator for assessing HCC progression by Response Evaluation Criteria in Solid Tumors (RECIST) standards, reflects poor prognosis, heightened metastasis risk, and significantly compromises the QOL of patients.[71] Notably, the combination group exhibited a significant reduction in average ascites volume compared to those of both the α-PD-1

https://doi.org/10.1021/acsnano.3c07885
ACS Nano 2023, 17, 23829−23849

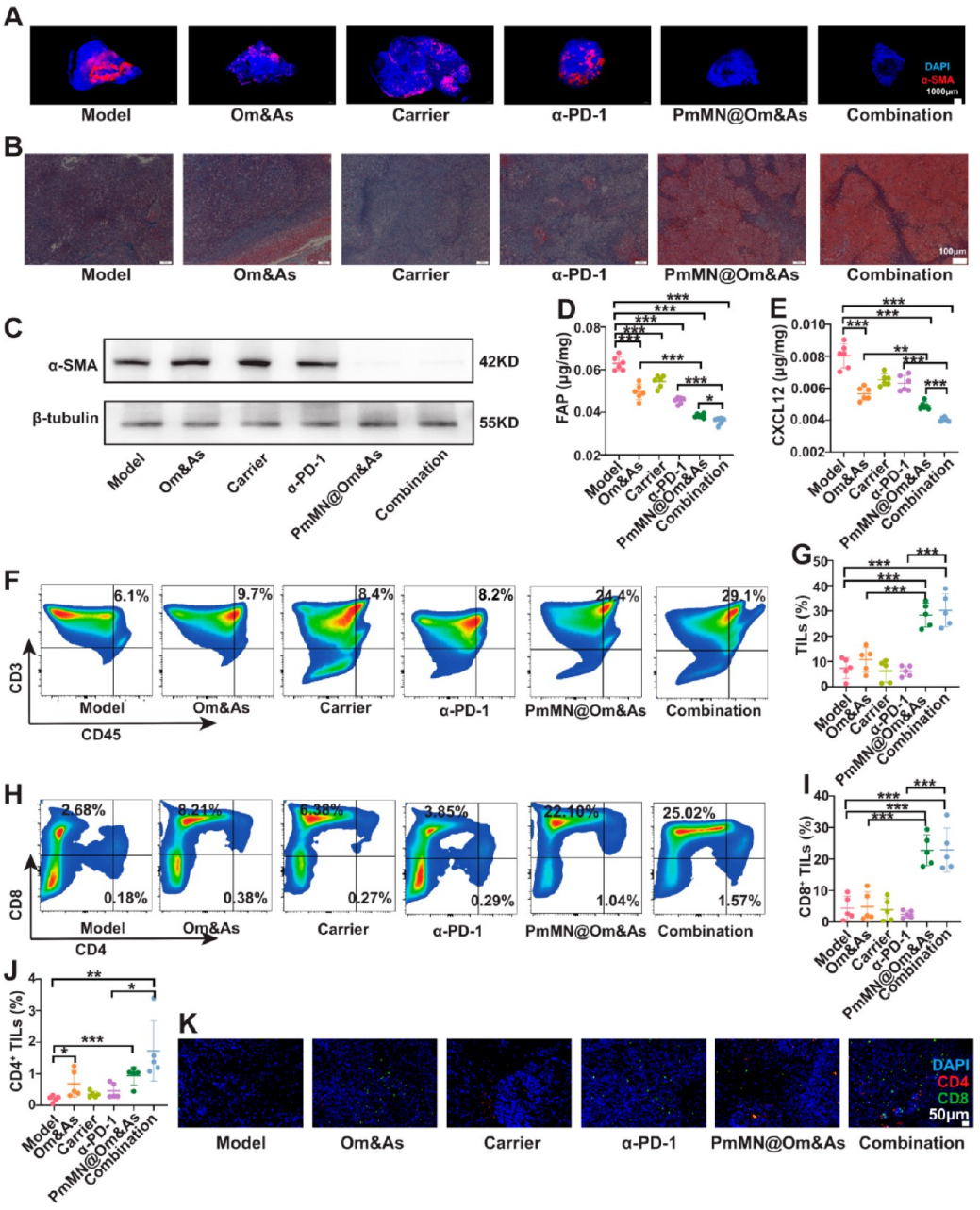

Figure 6. Effect of PmMN@Om&As on the upregulated levels of TILs by inhibiting the activation of CAFs. The activation of CAFs in tumor tissues was shown by α-SMA staining (scale bar = 1000 μm) (A). Collagen secreted by CAFs into tumor tissue was shown by Masson staining (scale bar = 100 μm) (B). α-SMA (C), FAP, (D), and CXCL12 (E) in tumor tissues were determined by WB and ELISA (n = 6), respectively. Levels of total TILs (F, G), $CD4^+$ (H, J, K), and $CD8^+$ TILs (H, I, K) were shown by flow cytometry (n = 5) and immunofluorescence staining (scale bar = 50 μm). Data are represented as the means ± SD $^*p < 0.05$, $^{**}p < 0.01$, $^{***}p < 0.001$, two-tailed Student's t test.

and model groups (Figure 5M). This demonstrated that PmMN@Om&As not only augmented the anti-HCC potency of α-PD-1 but also improved the QOL of the mice. Moreover, survival experiments indicate that mice in the combination therapy group attained the longest median survival (38 days) (Figure 5N), suggesting that combination therapy effectively prolongs the survival duration of patients with HCC.

The aforementioned results collectively establish the capacity of the combination strategy involving PmMN@Om&As and α-PD-1 to significantly enhance the anti-HCC effects of α-PD-1, while concurrently ameliorating the QOL and survival outcomes in the experimental mice. In our study, α-PD-1 was not completely devoid of antitumor efficacy but rather exhibited suboptimal therapeutic outcomes, which was consistent with published reports.[18,20] However, our comprehensive combination therapeutic approach substantially enhances the antitumor effect of α-PD-1, rendering it of pivotal clinical importance for the treatment of HCC.

Effect of PmMN@Om&As on Upregulating the Expression of TILs by Inhibiting the Activation of CAFs. The antitumor efficacy of α-PD-1 is closely dependent on the abundance of TILs. The infiltration of TILs is regulated by various factors such as CAFs, tumor vessels, and myeloid-derived suppressor cells. Among these factors, CAFs exert a

https://doi.org/10.1021/acsnano.3c07885
ACS Nano 2023, 17, 23829−23849

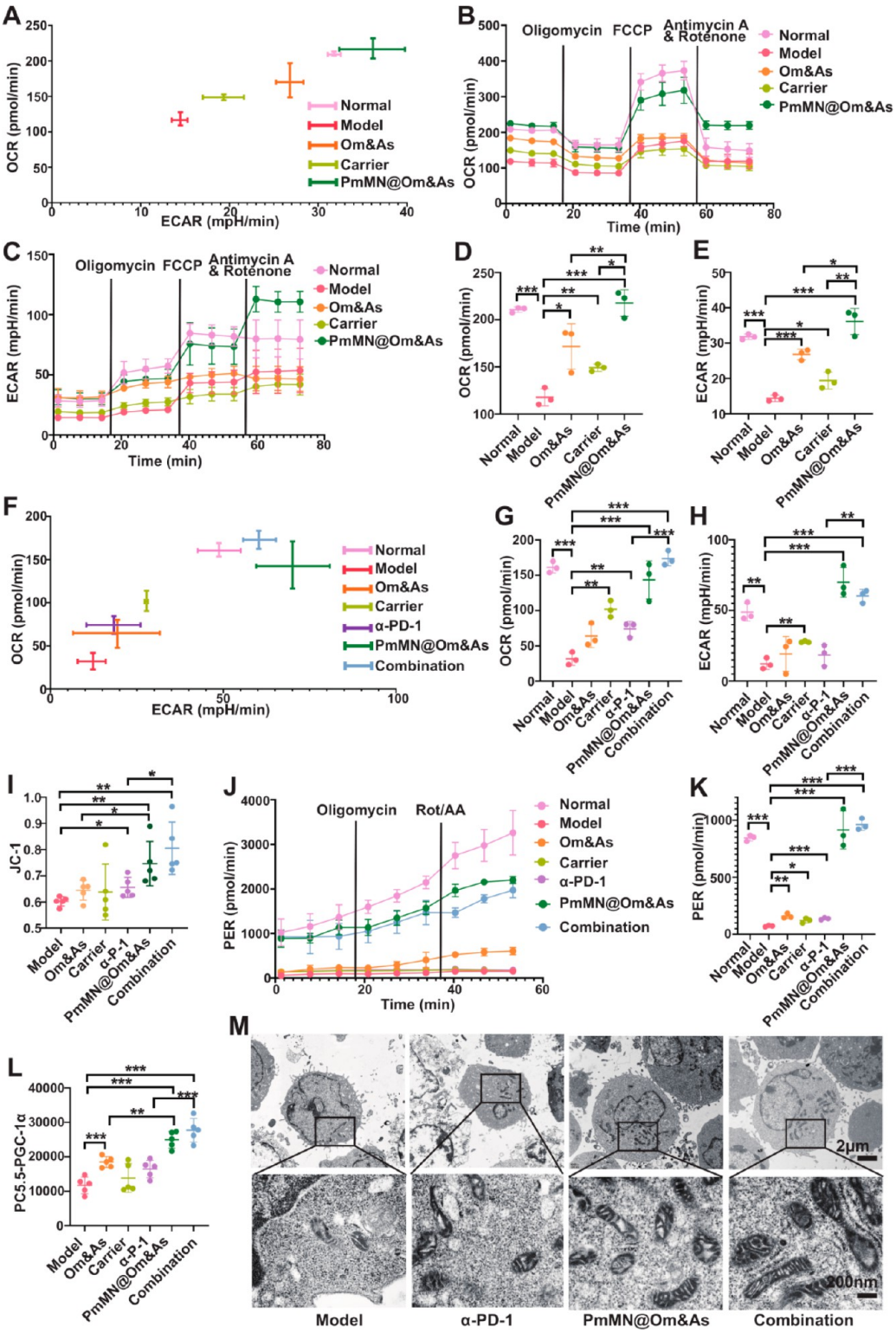

Figure 7. Effect of PmMN@Om&As on regulated mitochondrial normalization. Role of Om&As, carrier (PmMN), and PmMN@Om&As on the mitochondrial respiration of TILs *in vitro* (A) (n = 3). OCRs (B, D) and ECARs (C, E) of TILs *in vitro* were measured using the Seahorse XF^{e}96 analyzer (n = 3). Role of Om&As, carrier (PmMN), α-PD-1, PmMN@Om&As, and combination therapy on mitochondrial respiration of TILs *in vivo* (F) (n = 3). The OCRs (G) and ECARs (H) of TILs *in vivo* were measured by the Seahorse XF^{e}96 analyzer (n = 3). The mitochondrial membrane potential of TILs was determined by flow cytometry (n = 5) (I). The PER of TILs *in vivo* was measured by the Seahorse XF^{e}96 analyzer (n = 3) (J, K). The expression of PFC-1α in TILs was visualized by flow cytometry (n = 5) (L). Mitochondria of TILs were observed by TEM (scale bar 1 = 2 μm; scale bar 2 = 200 nm) (M). Data are represented as the means ± SD *p < 0.05, **p < 0.01, ***p < 0.001, two-tailed Student's t test.

https://doi.org/10.1021/acsnano.3c07885
ACS Nano 2023, 17, 23829−23849

considerable effect on the HCC microenvironment primarily due to the prevalence of cirrhosis in most patients with HCC.[72]

Activated CAFs are primarily characterized by upregulated expression of α-smooth muscle actin (α-SMA).[45,68] Immunofluorescence staining revealed a downregulated α-SMA expression in the tumor tissues of mice treated with combination therapy and PmMN@Om&As, indicating the ability of PmMN@Om&As to inhibit CAFs activation. This result was also supported by Western blotting analysis (Figure 6A, 6C). Activated CAFs can downregulate the expression of TILs by secreting collagen, FAP, and CXCL12, thereby decreasing the efficacy of PD-1 inhibitors. Masson staining showed that the model group exhibited abundant collagen deposition, whereas the PmMN@Om&As group and the combination group exhibited significantly less collagen deposition in tumor tissues (Figure 6B). This suggested that PmMN@Om&As can suppress collagen secretion via CAFs. ELISA results indicate that the levels of FAP and CXCL12 in the combination group were significantly lower than those in the model group and α-PD-1 group (Figure 6D, 6E), indicating that PmMN@Om&As can inhibit FAP and CXCL12 secretion via CAFs. Kobayashi et al. reported that activated CAFs can contribute to the abnormal proliferation of tumor blood vessels, impeding TIL infiltration into the tumor microenvironment.[25] Consequently, we performed an analysis of tumor vessel density using anti-CD31 labeling and found that the combination group exhibited the lowest CD31 in tumor tissues (Figure S4), suggesting that the combination therapy exhibits a beneficial effect in normalizing tumor blood vessels. Therefore, improved vascular normalization facilitated increased levels of TILs and improved the efficacy of α-PD-1 treatment.

We performed flow cytometry analysis to evaluate the abundance of TILs in the HCC tissue. The result indicates that treatment with α-PD-1 alone did not significantly change the number of $CD3^+$ TILs. However, $CD3^+$ TILs increased by 4.10-fold ($p < 0.001$) after undergoing combination therapy. Besides, compared with the model group, the PmMN@Om&As group also exhibited a significantly higher level of $CD3^+$ TILs (Figure 6F, G), indicating that PmMN@Om&As can increase the total TILs level. Furthermore, we evaluated the levels of the $CD8^+$ and $CD4^+$ TILs subpopulations. The results of flow cytometry and immunofluorescence showed a significant increase in $CD8^+$ TILs and $CD4^+$ TILs in the combination group compared with those in the model group (Figure 6H−K). However, no significant difference was found between the α-PD-1 group and the model group. This suggested that combination therapy upregulated the expression of $CD8^+$ TILs and $CD4^+$ TILs at the same time, which improved the effectiveness of α-PD-1. Interestingly, our findings revealed a considerable increase in T lymphocyte levels of the ascites of the combination group (Figure S5, F). This observation elucidated the mechanism behind the significantly decreased volume of ascites in the combination therapy group compared with the model groups.

Collectively, these results indicate that PmMN@Om&As upregulated the expression of TILs by inhibiting the activation of CAFs, which then improved the anti-HCC effect of the combination therapy of PmMN@Om&As and α-PD-1.

Effect of PmMN@Om&As on improving the activity of TILs by regulating mitochondrial normalization. Mitochondrial dysfunction attenuates the activity of TILs, hampering the anti-HCC effect of PD-1 inhibitor.[73,74] We showed that Om and As can enhance mitochondrial function and the activity of TILs *in vitro*. To determine whether PmMN@Om&As improved the activity of TILs by regulating mitochondrial functions *in vivo*, we obtained TILs from HCC tissues using MACS technology and assessed the mitochondrial function of TILs using the seahorse system.

Mitochondria produce ATP via aerobic and anaerobic respiration, and ATP provides energy for cellular activities. The results of the seahorse system indicate that the OCR and ECAR of TILs in the model group were significantly lower than those in the normal T lymphocytes of the homologous mouse spleens (Figure 7A−H), which confirmed that both aerobic and anaerobic respiratory functions of TILs were impaired.[29,74] The PmMN@Om&As group showed higher OCR and ECAR values compared with the model group, whereas the combination group exhibited even higher OCR and ECAR values than the α-PD-1 group (Figure 7F−H). These results suggested PmMN@Om&As could increase the aerobic and anaerobic respiration rate of TILs, which improved the efficacy of combination therapy. The ECARs of the PmMN@Om&As group and combination group were higher than those of the normal group because TILs were exposed to the hypoxic tumor microenvironment and their anaerobic respiration was activated. The OCR and ECAR of TILs in the Om&As group increased *in vitro* (Figure 7A-E) but did not show obvious changes *in vivo* (Figure 7F−H); however, those in the PmMN@Om&As group were significantly increased (Figure 7A−H) because the PmMN@Om&As improved the biodistribution and bioavailability of Om&As. Interestingly, the blank carrier also increased the aerobic and anaerobic respiration rate of TILs to a certain extent (Figure 7F, G), which was because the $Fe^{2+/3+}$ of the blank carrier may participate in the electron transfer process of mitochondrial respiration to increase aerobic respiration.[75] This result indicates that carriers played a role in codelivered Om&As and also synergistically increased mitochondrial respiration with Om&As (Figure 7F, G).

Mitochondrial membrane potential is an important factor that affects ATP production efficiency. The intracellular ATP level directly affects the anti-HCC function of TILs.[76] Herein, we used JC-1 as a fluorescent probe to evaluate the mitochondrial membrane potential of TILs and found that the mitochondrial membrane potential of TILs was significantly increased after treatment with PmMN@Om&As (Figure 7I). This result suggested that PmMN@Om&As exhibited the potential to accelerate the efficiency of ATP production of TILs. To validate this conclusion, proton efflux rate (PER) was used to determine the real-time ATP production efficiency of TILs. We found that TILs in the model group exhibited significantly lower PER than those in the normal group *in vivo* (Figure 7J, K), confirming that the ATP production efficiency of TIL mitochondria was inhibited by the tumor microenvironment. The PER of the PmMN@Om&As group was 12.56-fold ($p < 0.001$) higher than that of the model group *in vivo* and that of the combination group was 7.00-fold ($p < 0.001$) higher than that of the α-PD-1 group *in vivo* (Figure 7J, K). These results suggest that PmMN@Om&As can increase the ATP production of TILs, which can increase the anti-HCC activity of TILs and further improve the efficacy of combination therapy. Furthermore, although both Om&As and blank carrier raised the PER of TILs to a certain extent, the PER of the PmMN@Om&As group was much

https://doi.org/10.1021/acsnano.3c07885
ACS Nano 2023, 17, 23829−23849

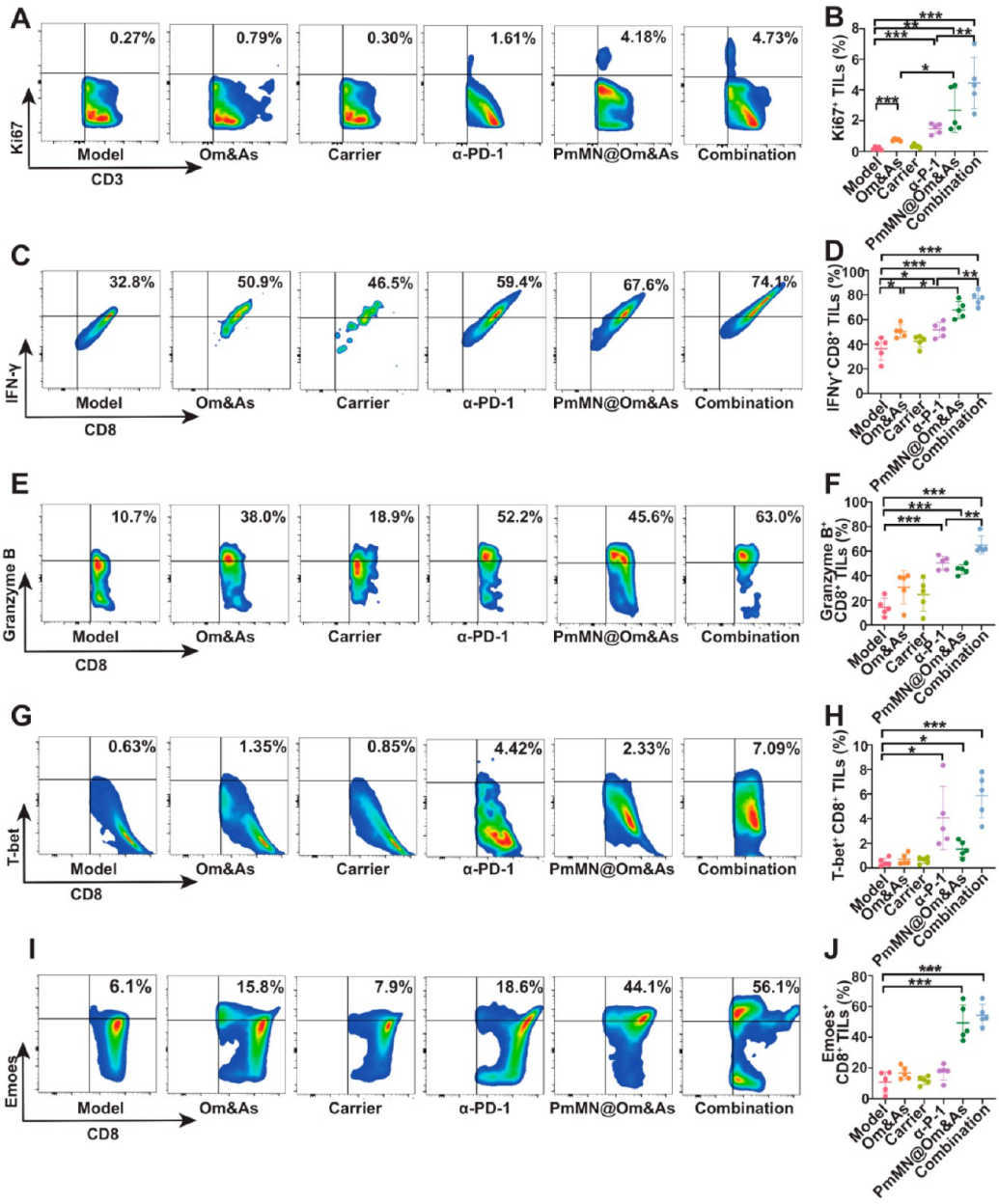

Figure 8. Effect of PmMN@Om&As on the increased activity of TILs. The proportion of Ki67$^+$ TILs in the total TILs was shown by flow cytometry (n = 5) (A, B). The proportion of IFN-γ^+ (C, D), Grazyme B$^+$ (E, F), T-bet$^+$ (G, H), and Emoes$^+$ TILs (I, J) in CD8$^+$ TILs was shown by flow cytometry (n = 5). Data are represented as the means ± SD *p < 0.05, **p < 0.01, ***p < 0.001, two-tailed Student's t test.

higher than that of the Om&As group and blank carrier group *in vivo* (Figure 7J, K), indicating that the carrier and Om&As can synergistically improve mitochondrial function.

The damaged structure of TIL mitochondria is an important cause of mitochondrial dysfunction.[28] PGC-1α was a key factor regulating mitochondrial biogenesis. Nicole et al. showed that the upregulation of PGC-1α can repair the structure of mitochondria and increase the activities of TILs.[29,74] We found that the expression of PGC-1α in TILs of the PmMN@Om&As group and combination group were significantly higher than those of the model group and α-PD-1 group (Figure 7L). TEM results also indicate that the TILs mitochondria in the PmMN@Om&As group and combination group had a larger volume and more cristae (Figure 7M, Figure S6), indicating a better mitochondrial function in these TILs. The aforementioned results indicate that PmMN@Om&As repaired the structure of mitochondria by upregulating PGC-1α, facilitating the anti-HCC effect of combination therapy.

We then evaluated the activity of TILs. Ki67 was used to determine the proliferation of TILs. The results indicate a substantial increase in the proportion of Ki67$^+$ cells in TILs of the PmMN@Om&As group compared with those of the model group. Furthermore, the combination group exhibited a significantly higher proportion of Ki67$^+$ cells in TILs than in the α-PD-1 group (Figure 8A, B). These results indicate that PmMN@Om&As can increase the proliferation of TILs, which was supported by the CCK8 assay (Figure S7B). In addition, PmMN@Om&As exhibited different effects on CAFs and H22 cells, showing an inhibitory effect on cellular activity (Figure S7A, C). However, the half-maximal inhibitory concentration (IC_{50}) of PmMN@Om&As for CAFs was 1.93 μg/mL, while the IC_{50} of PmMN@Om&As for H22 was 27.98 μg/mL,

https://doi.org/10.1021/acsnano.3c07885
ACS Nano 2023, 17, 23829−23849

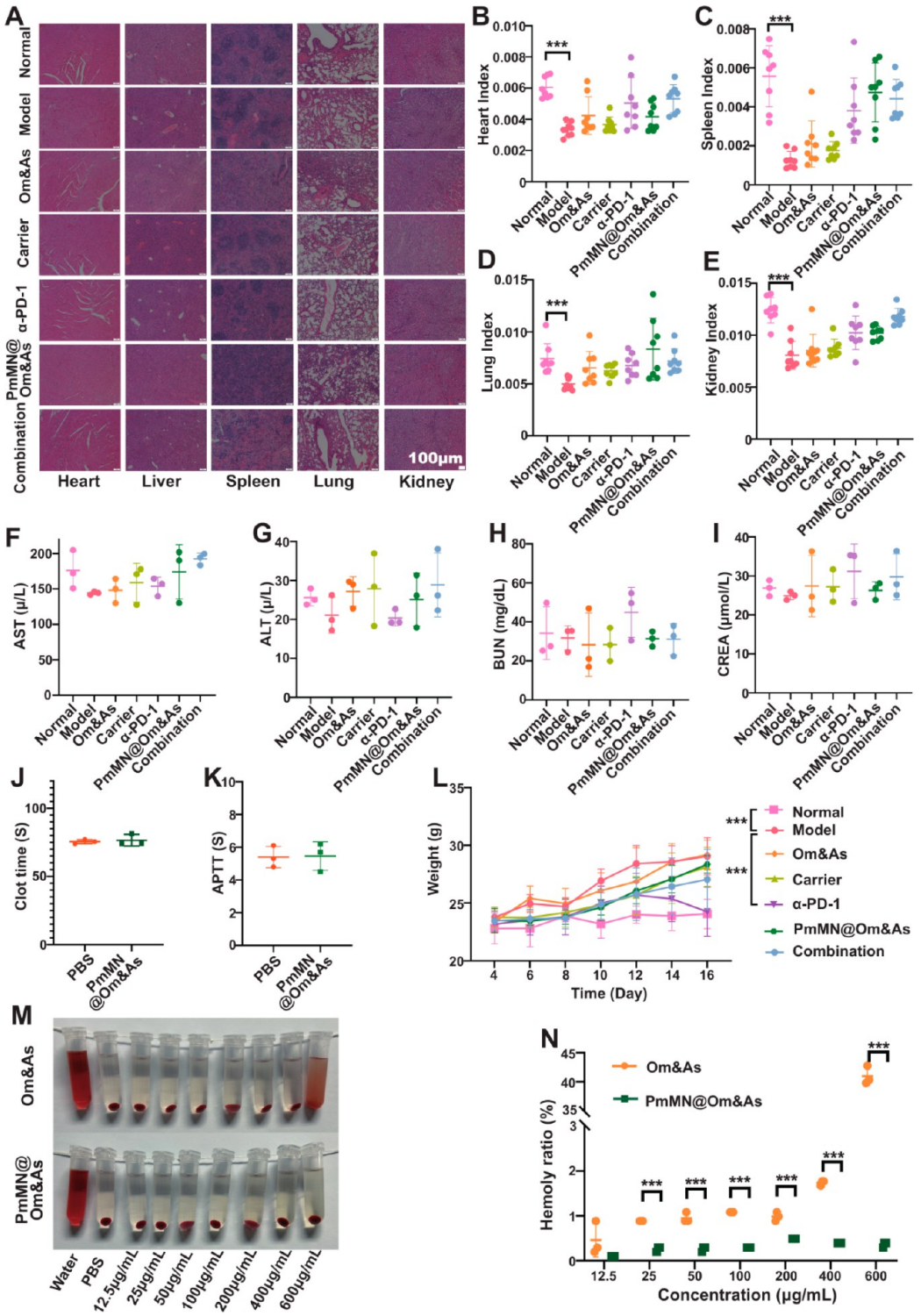

Figure 9. Safety evaluation of PmMN@Om&As. Sections of internal organs were used to observe the effect of drugs in mice (A). Heart index (B), spleen index (C), lung index (D), and kidney index (E) of mice were measured and analyzed (n = 5). AST (F), ALT (G), BUN (H), and CREA (I) were used to evaluate the liver and kidney function of mice (n = 3). Coagulation time (J) and APTT (K) were measured to evaluate the effect of PmMN@Om&As on the coagulation function of mice (n = 3). The body weights of mice in each group were monitored and recorded during treatment (n = 8) (L). The hemolytic properties of Om&As and PmMN@Om&As were tested and statistical (n = 3) (M, N). Data are represented as the means ± SD *p < 0.05, **p < 0.01, ***p < 0.001, two-tailed Student's t test.

which suggested that the inhibitory effect of PmMN@Om&As on CAFs was stronger than on H22. Consequently, the antitumor mechanism of PmMN@Om&As mainly relied on acting CAFs and TILs, rather than direct cytotoxicity against tumor cells.

Besides the proliferative activity, the antitumor activity of TILs was also determined. $CD8^+$ TILs kill tumors by secreting IFN-γ and granzyme B.[77] Flow cytometry showed that α-PD-1 increased the proportions of IFN-γ^+ and granzyme B^+ cells in $CD8^+$ TILs to a certain degree, which is consistent with the

https://doi.org/10.1021/acsnano.3c07885
ACS Nano 2023, 17, 23829−23849

study by Shi et al.[78] However, the regulatory capacity of α-PD-1 on IFN-γ$^+$ and granzyme B$^+$ TILs differentiation was found to be limited, attenuating its ability to achieve the desired therapeutic efficacy. Nevertheless, the combination group exhibited substantially higher proportions of IFN-γ$^+$ and granzyme B$^+$ cells compared with those in the α-PD-1 group, as evidenced by the results (Figure 8C−F; Figure S7D), and those in the PmMN@Om&As group were much higher than those in the model group. These results indicate that PmMN@Om&As can increase the anti-HCC effect of combination therapy by increasing the differentiation degree of CD8$^+$ TILs to IFN-γ$^+$ and granzyme B$^+$ cells. Furthermore, the proportions of T-bet$^+$ and Emoes$^+$ cells in CD8$^+$ TILs are positively correlated with the antitumor ability of CD8$^+$ TILs.[79] Flow cytometry results indicate that α-PD-1 increased the proportion of T-bet$^+$ cells in CD8$^+$ TILs, whereas PmMN@Om&As increased the proportion of Emoes$^+$ cells in CD8$^+$ TILs. In the combination group, the proportions of T-bet$^+$ cells and Emoes$^+$ cells in CD8$^+$ TILs were distinctly increased (Figure 8G−J), suggesting that combined PmMN@Om&As with α-PD-1 can induce differentiations of both T-bet$^+$ and Emoes$^+$ cells in CD8$^+$ TILs.

Altogether, the above-mentioned results suggested that PmMN@Om&As can increase the activity of TILs, thereby improving the anti-HCC effect of PD-1 inhibitors, which was achieved by regulating the mitochondrial functions of TILs.

Safety of the Combination Therapy of PmMN@Om&As and α-PD-1. Tissue sections and organ indices were used to evaluate the biosafety of the combination therapy of PmMN@Om&As and α-PD-1. The results of tissue sections revealed no damage to the organs of the mice (Figure 9A). The organ indices of the model group were significantly lower than those of the normal group, but those of the PmMN@Om&As group, α-PD-1 group, and combination group were not significantly different from the normal group (Figure 9B−E). This indicates that the combination therapy exhibited a good safety profile and reduced the burden of the tumor on the body.

Biochemical results indicate that combination therapy of PmMN@Om&As and α-PD-1 did not cause hepatotoxicity or nephrotoxicity (Figure 9F−I). In the routine blood test results, both the α-PD-1 group and the combination group exhibited a significant increase in white cells. However, the PmMN@Om&As group was not significantly different from the normal group, which may be caused by α-PD-1 (Figure S8A). This result is consistent with the report of Liu et al. The increased levels of white cells contribute to the antitumor effect.[80] α-PD-1 can also increase the platelet levels (Figure S8F), thus increasing the risk of thrombosis. However, the platelet levels were not increased in the combination group (Figure S8F), suggesting that PmMN@Om&As can eliminate the risk of α-PD-1-induced thrombosis.

To investigate whether the Pm coating affected coagulation function, we investigated the clotting time and partial prothrombin time in mice. The results indicate that PmMN@Om&As did not affect the coagulation function of mice (Figure 9J, K). Astragaloside IV could cause hemolysis but PmMN@Om&As could not, indicating that PmMN@Om&As can reduce the hemolytic risk of astragaloside IV (Figure 9M, N).

By measuring the body weight of mice, we found that HCC mice exhibited a faster trend of weight gain than normal mice except for the mice in the α-PD-1 group, which may be due to ascites (Figure 9L). Notably, mice in the α-PD-1 group exhibited more ascites and significantly lower body weight than the combination group (Figure 5M). However, body weight in the PmMN@Om&As group and combination group were not significantly different. This phenomenon indicates that α-PD-1 may reduce the QOL of mice, which can be addressed by using combination therapy with PmMN@Om&As.

Altogether, the above-mentioned results indicate that combination therapy exhibits credible safety.

CONCLUSION

To summarize, a magnetic MOF nanoplatform with Pm coating was developed to deliver Om and As into the microenvironment of HCC. This was used synergistically with PD-1 against HCC. PmMN@Om&As can accelerate cellular uptake and evade MPS clearance via the CD47 of Pm. PmMN@Om&As can also target HCC tissues under a magnetic field and survive in the HCC microenvironment via the interaction between Pm and collagen that are secreted by CAFs, thereby exerting long-term effects. The reductive and acidic microenvironment of HCC accelerates the disintegration of PmMN@Om&As, thereby releasing Om&As. Furthermore, Om upregulated the infiltration of TILs by inhibiting the activation of CAFs but improved the activities of TILs by regulating mitochondrial normalization. Interestingly, the $Fe^{2+/3+}$ in PmMN@Om&As could synergize with Om&As to improve mitochondrial function. Lastly, combining PmMN@Om&As with α-PD-1 significantly improved the anti-HCC effect of α-PD-1, prolonged the survival and QOL of HCC mice, and exhibited good safety. This study provides a promising approach to improve the effectiveness of PD-1 inhibitors by simultaneously increasing the level and activity of TILs, which offers a promising strategy to improve the efficacy of clinical HCC immunotherapy.

Materials. Sodium acetate, HNO_3, and HF were purchased from Nanjing Reagent Co., Ltd. (Nanjign, China). Sodium acrylate and astragaloside IV were purchased from Yuanye Bio-Technology Co., Ltd. (Shanghai, China). Oxymatrine was purchased from Chunqiu Biomedical Technology (Nanjign, China). $FeCl_3{\cdot}H_2O$, EDTA-2Na, and C6 were purchased from Aladdin Reagent Co., Ltd. (Shanghai, China). Diethylene glycol and DiD were provided by Sigma-Aldrich Co., Ltd. (Missouri, America). BTC was provided by Rhawn Chemical Reagent (Shanghai, China). Methanol was provided by Xilong Scientific (Shantou, China). RIPA lysis buffer, protease inhibitor cocktail, phosphatase inhibitor cocktail, and loading buffer were purchased from Glpbio Co., Ltd. (California, America). Polyvinylidene fluoride membranes were purchased from Bio-Rad Laboratories Co., Ltd. (California, America). *In vivo* mAb antimouse CD47 and *In vivo* mAb antimouse PD-1 were purchased from BioXcell Co., Ltd. (New Hampshire, America). Antimouse CD47 and antirabbit IgG were obtained from Abmart Shanghai Co., Ltd. (Shanghai, China). D-Luciferin potassium salt was obtained from BioFroxx Co., Ltd. (Germany). Brilliant Violet 421 antimouse CD45, PE/Cyanine7 antimouse CD3, FITC antimouse CD4 Antibody, Alexa Fluor 700 antimouse CD8a, APC/T-bet monoclonal antibody, PE/eomes menocional antibody, FITC antimouse CD11b, Alexa Fluor 700 antimouse F4/80, Purified antimouse CD16/32 Antibody and Ki67 were obtained from Biolegend Co., Ltd. (California, America). PE/IFN gamma Monoclonal Antibody was purchased from eBioscience Co., Ltd. (California, America). Antimouse PGC-1α Antibody and

https://doi.org/10.1021/acsnano.3c07885
ACS Nano 2023, 17, 23829−23849

Goat Anti-Rabbit IgG H&L (Alexa Fluor 488) were purchased from Abcam Co., Ltd. (Cambridge, England).

Cell Lines and Animals. NIH3T3, CTLL-2, and H22 cells were obtained from the National Collection of Authenticated Cell Culture (Shanghai, China). H22-Luc cells were provided by China Pharmaceutical University (Nanjing, China). NIH3T3, CTLL-2, H22, and H22-Luc cells were cultured in a cell incubator at 37 °C under 5% CO_2. The medium of NIH3T3 was DMEM with 10% fetal bovine serum (FBS), and the medium of CTLL-2, H22, and H22-Luc was RPMI 1640 with 10% FBS.

Male C57BL/6 mice (6−8 weeks old, 18−20 g) were provided by GemPharmatech LLC. (Nanjing, China). All animal procedures were performed in accordance with the Guidelines for Care and Use of Laboratory Animals of the Jiangsu Province Academy of Traditional Chinese Medicine.

Preparation of PmMN@Om&As. 3.75 g of sodium acetate, 3.75 g of sodium acrylate, and 1.875 g of $FeCl_3{\cdot}H_2O$ were dissolved in 150 mL of diethylene glycol, stirred for 24 h at room temperature, and then transferred into a Teflon-lined autoclave for heating at 190 °C for 10 h. After it was cooled to room temperature, it was centrifuged at 55000 rpm for 30 min. The precipitated fraction was retained as a Fe_3O_4 nanoparticles.

A 100 mg amount of Fe_3O_4 nanoparticles and 287.5 mg of BTC were dissolved in 50 mL of water which contained 2.5 mM HNO_3 and 0.075 mM HF, and then transferred into a Teflon-lined autoclave for heating at 150 °C for 4 h. MN was collected by a magnet.

400 mg of Om and 200 mg of As were dissolved in 100 mL of methanol and ultrasonic processed for 10 min at room temperature. 50 mg of MN were heated to 150 °C to activate the pores, and then transferred into the methanol which contained Om&As, and stirred for 12 h at room temperature. After stirring, MN@Om&As was collected by a magnet.

C57BL/6 mice blood was drawn into 1.5 g/L EDTA-2Na. Platelets were collected using a platelet separation kit (Haoyang TBD science). Pm was obtained by repeatedly freezing and thawing platelet membranes between −80 °C and room temperature. For the synthesis of PmMN@Om&As, Pm (2 mg/mL) was mixed with MN@Om&As (2 mg/mL) at membrane-to-core weight ratios of 1:2, and the mixture was then sonicated at 200 w for 10 min (sonication for 1 s, intervals for 2 s) on ice. Finally, PmMN@Om&As was collected by a magnet.

Characterization of PmMN@Om&As. The morphology was examined using SEM (LEO 1530VP, LEO Election Microscopy Ltd.) and TEM (Tecnai G2 F20 S-Twin, FEI). The size and zeta potentials of PmMN@Om&As were determined by DLS using a Zeta Potential/Particle Sizer (Zetasizer Nano ZS, Malvern Panalytical). Surface area, pore size, and pore volume were determined by using a micromeritics surface area analyzer (TriStar II 3020, Micromeritics Instrument Corporation). Magnetic properties were determined by using a VSM (LakeShore7404, Lake Shore) and a NdFeB magnet. Crystal characteristics were determined by using an XRD (Max-2200PC, Rigakud).

The presence of membrane-associated proteins on the particles was verified by SDS-PAGE and WB. For the analysis, the Pm and PmMN@Om&As were first lysed in RIPA lysis buffer containing protease inhibitor cocktail and phosphatase inhibitor cocktail on ice for 5 min. Thereafter, the lysates were centrifuged at 13000× *g* for 5 min at 4 °C, the supernatant was then subjected to enhanced BCA protein assay (Thermo) for the quantification of the total protein. After that, the supernatant protein was mixed with loading buffer and heated at 100 °C for 5 min. An equivalent of 30 μg of protein per sample was loaded into each well of an 8% Tris/glycine SDS-poly acrylamide gelatin in an electrophoresis chamber system. For total imaging, the protein blots were stained with a protein staining kit (EnoGene). For WB analysis, the proteins were transferred to polyvinylidene fluoride membranes which were then blocked with 5% nonfat milk in TBST (Tris-HCl 50 mM, NaCl 150 mM, Tween 80 0.1%) for 1.5 h at room temperature. The blots were probed by antimouse CD47 at 4 °C and then incubated with the corresponding antirabbit IgG before the final visualization on film.

DLE and drug release profiles were determined by HPLC. The contents of Om and As in the methanol solution before (M1) and after (M2) drug loading was determined by HPLC. DLE was calculated by the ratio between the (M1 - M2) and the mass of PmMN@Om&As. PmMN@Om&As was placed in 4 solutions (neutral solution: pH7.4, 0.5% SDS-PBS; acidic solution: pH6.4, H_3PO_4-0.5% SDS-PBS, reductive solution: 10 mM GSH-0.5% SDS-PBS, reductive and acidic solution: 10 mM GSH-pH6.4, H_3PO_4-0.5% SDS-PBS) for drug release experiments. Solutions were collected at various times and replenished with fresh solutions. The collected solutions were concentrated 5× and detected by HPLC.

HPLC analysis was performed on an Agilent chromatographic system (1260, Agilent). The mobile phase involved a mixture of 0.3% phosphate buffer and acetonitrile (0−15 min, 90:10 v/v; 15−25 min, 90:10−45:55 v/v; 25−40 min, 45:55−20:80 v/v), pumped at a flow rate of 1 mL/min through the column (ZORBAXSB-C18, 5 μm, 250 mm × 4.6 mm).

CAFs and TILs Cells Models *in Vitro*. The CAFs cell model was established based on NIH3T3 cells. Briefly, CAFs were constructed by coincubating NIH3T3 cells with 5 ng/mL TGF-β1 for 48 h.

A TILs cell model was obtained by coculturing CTLL-2 cells and H22 cells. A total of 1×10^6 CTLL-2 cells were added to the lower transwell chamber (Corning), and 1×10^6 H22 cells were seeded in the upper chamber of the coculture system for 48 h.

Fluorescently Labeled PmMN@Om&As. 5 mg of C6 were dissolved in 10 mL of methanol and sonicated for 10 min at room temperature. Follow the method in "Preparation of PmMN@Om&As" to get MN@C6 and PmMN@C6. 5 mg DiD was dissolved in 5 mL of methanol and sonicated 10 min at room temperature. Follow the method in "Preparation of PmMN@Om&As" to get MN@DiD and PmMN@DiD. All the above operations were performed in a dark environment.

Cellular Uptake. CAFs, TILs, and H22 cells were seeded in a 6-well cell culture plate at a density of 1×10^5 cells/well and then incubated at 37 °C overnight. After different treatments, 4 °C PBS was used to terminate cellular uptake and DAPI was used to label cells. Fluorescence microscopy (IX-73, Olympus) was used to observe the cellular uptake of the different drugs. Cells were also collected, and the brightness of the fluorescence was counted using flow cytometry (CytoFLEX, Beckman).

The cellular drug uptake mechanism was reflected in competitive inhibition experiments. Briefly, after the cells were treated with sucrose, genistein, amiloride, and a low-temperature environment, different drugs were used to

https://doi.org/10.1021/acsnano.3c07885
ACS Nano 2023, 17, 23829−23849

coincubate with the cells. Further, flow cytometry was used to determine the efficiency of drug uptake by cells.

Immune Escape of PmMN@Om&As. The immune escape ability of PmMN@Om&As was verified by RAW264.7 cells *in vitro* and C57BL/6 mice *in vivo*. RAW264.7 cells were seeded in a six-well cell culture plate at a density of 1×10^5 cells/well and then incubated at 37 °C overnight. After different treatments, cells were collected and counted based on the brightness of the fluorescence using flow cytometry.

PmMN@C6 was coincubated with CD47 antibody for 12 h to block CD47 (Pm-BCD47). MN@C6, PmMN@C6, and Pm-BCD47 were injected intravenously into mice. After 4 h, the spleens of the mice were collected and processed into a single cell state. Antimouse F4/80 and antimouse CD11b were used to label macrophages, and flow cytometry was used to measure the efficiency of macrophages to phagocytose nanoparticles.

Adhesion of Collagen to PmMN@Om&As. Collagen-coated glass plates were placed in a flow cell, and a peristaltic pump was used to provide a constant flow rate to mimic the tumor blood flow. MN@C6 and PmMN@C6 were circulated with the solution in the flow cell for 10 min. The MN@C6 or PmMN@C6 remaining on the glass plate was observed by a fluorescence microscope.

Orthotopic Transplantation Tumor Model. Mice were randomly divided into different subgroups. 1×10^6 H22-Luc cells were transplanted into the livers of C57BL/6 mice. Bioluminescence imaging was performed using an IVIS Spectrum (PerkinElmer) instrument to exclude the mice that have no tumor.

***In Vivo* Fluorescence Imaging Study.** Equal doses of DiD, MN@DiD, and PmMN@DiD were injected via the tail vein into mice with HCC. Images were captured at different postinjection times (0.5, 1, 2, 3, 4, 6, 8, 10, and 24 h) by IVIS Spectrum. At 24 h after injection, mice were sacrificed, and the main organs (tumor, heart, liver, spleen, lung, and kidney) were harvested for *ex vivo* fluorescence imaging. Laser confocal microscopy was used to observe the distribution of drugs in tumor tissue.

***In Vivo* Antitumor Efficacy.** The orthotopic transplantation tumor model of HCC in C57BL/6 mice was established ($n = 8$) according to the description in "Orthotopic Transplantation Tumor Model". After 3 days, mice were treated respectively with PBS, Om&As (Om: 2 mg/kg; As: 1.5 mg/kg), blank carrier (15 mg/kg), and PmMN@Om&As (15 mg/kg) via intravenous administration every day. Mice in the α-PD-1 group and the combination group were injected with α-PD-1 (5 mg/kg) via intravenous administration every 4 days. At the end of the antitumor efficacy study, mice were sacrificed, and tumors were collected as well as weighed. Moreover, the tumors were sectioned. We stained these slices with HE, Ki67, and TUNEL to observe the histopathological changes. Apoptosis of tumor cells was measured by using flow cytometry. Survival experiments were also performed. Besides, ascites were collected and studied.

Flow Cytometry Analysis. We sacrificed mice and collected tumor tissues, which were digested at 37 °C in a buffer containing 1 mg/mL collagenase I, 1 mg/mL collagenase IV, 0.04 mg/mL DNAase, and 0.4 mg/mL HAase for 5 h. Subsequently, the mixtures were ground and filtered to collect the single cells. Single cells were labeled with antibodies and analyzed by using flow cytometry.

Western Blot Analysis. After treatment, tumor tissues were collected and lysed in RIPA lysis buffer containing protease inhibitor cocktail and phosphatase inhibitor cocktail, and then, it was prepared into a homogenate by using a grinder (Tissuelyser-L, Jingxin). The lysates were centrifuged at 13000× *g* for 5 min at 4 °C, and the supernatant was then subjected to enhanced BCA protein assay for the quantification of the total protein. Proteins were separated by SDS-PAGE and transferred to PVDF membranes. PVDF membranes were blocked with 5% nonfat milk and further incubated with the indicated primary antibodies overnight at 4 °C. Subsequently, it was incubated with HRP-conjugated secondary antibody for 1 h at room temperature and scanned with an Imaging analysis system (5200, Tanon).

ELISA Assay. FAP and CXCL12 in the samples were tested with ELISA kits.

TILs acquisition. TILs were obtained by a Pan T Cell Isolation Kit II (Miltenyi Biotec).

Measurement OCR, ECAR, and PER. A Seahorse XFe96 analyzer (Agilent) was used to measure the OCR, ECAR, and PER of TILs. Briefly, different groups of treated cells were seeded in a Seahorse XFe96 FluxPak culture microplate, and the plates were detected according to the manufacturer's instructions for the Seahorse XF Cell Mito stress test kit (Agilent).

ASSOCIATED CONTENT

Supporting Information

The Supporting Information is available free of charge at https://pubs.acs.org/doi/10.1021/acsnano.3c07885.

DLS, EDS, and stability results of PmMN@Om&As, magnetic response abilities of Fe_3O_4 and MN, EDS results of MN and MN@Om&As (Figure S1); cell uptake statistical analyses of CAFs and TILs, cell uptake results of H22 cells, immune escape statistical analyses of PmMN@Om&As, effects of CD47 on cellular uptake of CAFs and TILs (Figure S2); statistical analysis of tumors bioluminescence (Figure S3); CD31 staining results of tumors (Figure S4); results of T lymphocytes in mice ascites (Figure S5); TEM images of normal T lymphocytes mitochondria (Figure S6); CCK8 results of MN and PmMN@Om&As in CAFs, TILs, and H22 cells, granzyme B and CD8 staining results of tumors (Figure S7); blood routine examination results of mice (Figure S8); element content of MN, MN@Om&As, and PmMN@Om&As (Table S1). (PDF)

AUTHOR INFORMATION

Corresponding Authors

Jiege Huo − *Affiliated Hospital of Integrated Traditional Chinese and Western Medicine, Nanjing University of Chinese Medicine, Nanjing 210028, China; Jiangsu Clinical Innovation Center of Digestive Cancer of Traditional Chinese Medicine, Nanjing 210028, China*; Email: huojiege@hotmail.com

Yan Chen − *Affiliated Hospital of Integrated Traditional Chinese and Western Medicine, Nanjing University of Chinese Medicine, Nanjing 210028, China; Jiangsu Clinical Innovation Center of Digestive Cancer of Traditional Chinese Medicine, Nanjing 210028, China*; orcid.org/0000-0003-0864-1630; Email: ychen202@hotmail.com

https://doi.org/10.1021/acsnano.3c07885
ACS Nano 2023, 17, 23829−23849

Authors

Hong Guo − *Affiliated Hospital of Integrated Traditional Chinese and Western Medicine, Nanjing University of Chinese Medicine, Nanjing 210028, China; Multi-component of Traditional Chinese Medicine and Microecology Researh Center, Jiangsu Province Academy of Traditional Chinese Medicine, Nanjing 210028, China*

Yuping Liu − *Affiliated Hospital of Integrated Traditional Chinese and Western Medicine, Nanjing University of Chinese Medicine, Nanjing 210028, China; Multi-component of Traditional Chinese Medicine and Microecology Researh Center, Jiangsu Province Academy of Traditional Chinese Medicine, Nanjing 210028, China; Jiangsu Clinical Innovation Center of Digestive Cancer of Traditional Chinese Medicine, Nanjing 210028, China;* orcid.org/0000-0002-4691-4348

Xia Li − *Affiliated Hospital of Integrated Traditional Chinese and Western Medicine, Nanjing University of Chinese Medicine, Nanjing 210028, China; Multi-component of Traditional Chinese Medicine and Microecology Researh Center, Jiangsu Province Academy of Traditional Chinese Medicine, Nanjing 210028, China*

Hong Wang − *Affiliated Hospital of Integrated Traditional Chinese and Western Medicine, Nanjing University of Chinese Medicine, Nanjing 210028, China; Multi-component of Traditional Chinese Medicine and Microecology Researh Center, Jiangsu Province Academy of Traditional Chinese Medicine, Nanjing 210028, China*

Dengxuan Mao − *Affiliated Hospital of Integrated Traditional Chinese and Western Medicine, Nanjing University of Chinese Medicine, Nanjing 210028, China; Multi-component of Traditional Chinese Medicine and Microecology Researh Center, Jiangsu Province Academy of Traditional Chinese Medicine, Nanjing 210028, China*

Liangyin Wei − *Affiliated Hospital of Integrated Traditional Chinese and Western Medicine, Nanjing University of Chinese Medicine, Nanjing 210028, China; Multi-component of Traditional Chinese Medicine and Microecology Researh Center, Jiangsu Province Academy of Traditional Chinese Medicine, Nanjing 210028, China*

Xietao Ye − *Affiliated Hospital of Integrated Traditional Chinese and Western Medicine, Nanjing University of Chinese Medicine, Nanjing 210028, China; Multi-component of Traditional Chinese Medicine and Microecology Researh Center, Jiangsu Province Academy of Traditional Chinese Medicine, Nanjing 210028, China*

Ding Qu − *Affiliated Hospital of Integrated Traditional Chinese and Western Medicine, Nanjing University of Chinese Medicine, Nanjing 210028, China; Multi-component of Traditional Chinese Medicine and Microecology Researh Center, Jiangsu Province Academy of Traditional Chinese Medicine, Nanjing 210028, China;* orcid.org/0000-0002-1217-1865

Complete contact information is available at: https://pubs.acs.org/10.1021/acsnano.3c07885

Author Contributions

[‖]Hong Guo and Yuping Liu contributed equally to this work. Yan Chen and Jiege Huo designed the research. Hong Guo, Yuping Liu, Xia Li, Hong Wang, Dengxuan Mao, Liangyin Wei, and Xietao Ye performed experiments. All authors analyzed and interpreted the data. Hong Guo, Yuping Liu, and Ding Qu designed the figures. Yan Chen, Hong Guo, and Yuping Liu wrote the paper.

Notes

The authors declare no competing financial interest.

ACKNOWLEDGMENTS

This work was supported financially by the National Natural Science Foundation of China (82173985), the Science and Technology Plan Project of Jiangsu Provincial (BE2021754), the Special Project for the Development of Traditional Chinese Medicine Technology of Jiangsu Province (2020ZX15), and the Jiangsu Clinical Innovation Center of Digestive Cancer of Traditional Chinese Medicine (No. 2021.6)

REFERENCES

(1) Sperandio, R. C.; Pestana, R. C.; Miyamura, B. V.; Kaseb, A. O. Hepatocellular Carcinoma Immunotherapy. *Annual review of medicine* **2022**, *73*, 267−278.

(2) Craig, A. J.; von Felden, J.; Garcia-Lezana, T.; Sarcognato, S.; Villanueva, A. Tumour evolution in hepatocellular carcinoma. *Nature reviews. Gastroenterology & hepatology* **2020**, *17* (3), 139−152.

(3) Cheng, A. L.; Hsu, C.; Chan, S. L.; Choo, S. P.; Kudo, M. Challenges of combination therapy with immune checkpoint inhibitors for hepatocellular carcinoma. *Journal of hepatology* **2020**, *72* (2), 307−319.

(4) Gunasekaran, G.; Bekki, Y.; Lourdusamy, V.; Schwartz, M. Surgical Treatments of Hepatobiliary Cancers. *Hepatology (Baltimore, Md.)* **2021**, *73* (S1), 128−136.

(5) Reig, M.; Forner, A.; Rimola, J.; Ferrer-Fabrega, J.; Burrel, M.; Garcia-Criado, A.; Kelley, R. K.; Galle, P. R.; Mazzaferro, V.; Salem, R.; Sangro, B.; Singal, A. G.; Vogel, A.; Fuster, J.; Ayuso, C.; Bruix, J. BCLC strategy for prognosis prediction and treatment recommendation: The 2022 update. *Journal of hepatology* **2022**, *76* (3), 681−693.

(6) Foerster, F.; Gairing, S. J.; Müller, L.; Galle, P. R. NAFLD-driven HCC: Safety and efficacy of current and emerging treatment options. *Journal of hepatology* **2022**, *76* (2), 446−457.

(7) Lee, T. K.; Guan, X. Y.; Ma, S. Cancer stem cells in hepatocellular carcinoma - from origin to clinical implications. *Nature reviews. Gastroenterology & hepatology* **2022**, *19* (1), 26−44.

(8) Cheng, A. L.; Kang, Y. K.; Chen, Z.; Tsao, C. J.; Qin, S.; Kim, J. S.; Luo, R.; Feng, J.; Ye, S.; Yang, T. S.; Xu, J.; Sun, Y.; Liang, H.; Liu, J.; Wang, J.; Tak, W. Y.; Pan, H.; Burock, K.; Zou, J.; Voliotis, D.; Guan, Z. Efficacy and safety of sorafenib in patients in the Asia-Pacific region with advanced hepatocellular carcinoma: a phase III randomised, double-blind, placebo-controlled trial. *Lancet. Oncology* **2009**, *10* (1), 25−34.

(9) He, M.; Li, Q.; Zou, R.; Shen, J.; Fang, W.; Tan, G.; Zhou, Y.; Wu, X.; Xu, L.; Wei, W.; Le, Y.; Zhou, Z.; Zhao, M.; Guo, Y.; Guo, R.; Chen, M.; Shi, M. Sorafenib Plus Hepatic Arterial Infusion of Oxaliplatin, Fluorouracil, and Leucovorin vs Sorafenib Alone for Hepatocellular Carcinoma With Portal Vein Invasion: A Randomized Clinical Trial. *JAMA oncology* **2019**, *5* (7), 953−960.

(10) Li, Q. J.; He, M. K.; Chen, H. W.; Fang, W. Q.; Zhou, Y. M.; Xu, L.; Wei, W.; Zhang, Y. J.; Guo, Y.; Guo, R. P.; Chen, M. S.; Shi, M. Hepatic Arterial Infusion of Oxaliplatin, Fluorouracil, and Leucovorin Versus Transarterial Chemoembolization for Large Hepatocellular Carcinoma: A Randomized Phase III Trial. *Journal of clinical oncology: official journal of the American Society of Clinical Oncology* **2022**, *40* (2), 150−160.

(11) Hsu, C. L.; Ou, D. L.; Bai, L. Y.; Chen, C. W.; Lin, L.; Huang, S. F.; Cheng, A. L.; Jeng, Y. M.; Hsu, C. Exploring Markers of Exhausted CD8 T Cells to Predict Response to Immune Checkpoint Inhibitor Therapy for Hepatocellular Carcinoma. *Liver cancer* **2021**, *10* (4), 346−359.

(12) Sangro, B.; Sarobe, P.; Hervás-Stubbs, S.; Melero, I. Advances in immunotherapy for hepatocellular carcinoma. *Nature reviews. Gastroenterology & hepatology* **2021**, *18* (8), 525−543.
(13) Hoos, A. Development of immuno-oncology drugs - from CTLA4 to PD1 to the next generations. *Nature reviews. Drug discovery* **2016**, *15* (4), 235−47.
(14) Callahan, M. K.; Postow, M. A.; Wolchok, J. D. Targeting T Cell Co-receptors for Cancer Therapy. *Immunity* **2016**, *44* (5), 1069−78.
(15) Yau, T.; Park, J. W.; Finn, R. S.; Cheng, A. L.; Mathurin, P.; Edeline, J.; Kudo, M.; Harding, J. J.; Merle, P.; Rosmorduc, O.; Wyrwicz, L.; Schott, E.; Choo, S. P.; Kelley, R. K.; Sieghart, W.; Assenat, E.; Zaucha, R.; Furuse, J.; Abou-Alfa, G. K.; El-Khoueiry, A. B.; Melero, I.; Begic, D.; Chen, G.; Neely, J.; Wisniewski, T.; Tschaika, M.; Sangro, B. Nivolumab versus sorafenib in advanced hepatocellular carcinoma (CheckMate 459): a randomised, multicentre, open-label, phase 3 trial. *Lancet. Oncology* **2022**, *23* (1), 77−90.
(16) Llovet, J. M.; Castet, F.; Heikenwalder, M.; Maini, M. K.; Mazzaferro, V.; Pinato, D. J.; Pikarsky, E.; Zhu, A. X.; Finn, R. S. Immunotherapies for hepatocellular carcinoma. *Nature reviews. Clinical oncology* **2022**, *19* (3), 151−172.
(17) Bagchi, S.; Yuan, R.; Engleman, E. G. Immune Checkpoint Inhibitors for the Treatment of Cancer: Clinical Impact and Mechanisms of Response and Resistance. *Annual review of pathology* **2021**, *16*, 223−249.
(18) Kraehenbuehl, L.; Weng, C. H.; Eghbali, S.; Wolchok, J. D.; Merghoub, T. Enhancing immunotherapy in cancer by targeting emerging immunomodulatory pathways. *Nature reviews. Clinical oncology* **2022**, *19* (1), 37−50.
(19) Zou, W.; Wolchok, J. D.; Chen, L. PD-L1 (B7-H1) and PD-1 pathway blockade for cancer therapy: Mechanisms, response biomarkers, and combinations. *Science translational medicine* **2016**, *8* (328), 328rv4.
(20) Andrews, L. P.; Yano, H.; Vignali, D. A. A. Inhibitory receptors and ligands beyond PD-1, PD-L1 and CTLA-4: breakthroughs or backups. *Nature immunology* **2019**, *20* (11), 1425−1434.
(21) Wang, F.; Wei, X. L.; Wang, F. H.; Xu, N.; Shen, L.; Dai, G. H.; Yuan, X. L.; Chen, Y.; Yang, S. J.; Shi, J. H.; Hu, X. C.; Lin, X. Y.; Zhang, Q. Y.; Feng, J. F.; Ba, Y.; Liu, Y. P.; Li, W.; Shu, Y. Q.; Jiang, Y.; Li, Q.; Wang, J. W.; Wu, H.; Feng, H.; Yao, S.; Xu, R. H. Safety, efficacy and tumor mutational burden as a biomarker of overall survival benefit in chemo-refractory gastric cancer treated with toripalimab, a PD-1 antibody in phase Ib/II clinical trial NCT02915432. *Annals of oncology: official journal of the European Society for Medical Oncology* **2019**, *30* (9), 1479−1486.
(22) Kon, E.; Benhar, I. Immune checkpoint inhibitor combinations: Current efforts and important aspects for success. *Drug resistance updates: reviews and commentaries in antimicrobial and anticancer chemotherapy* **2019**, *45*, 13−29.
(23) Daly, R. J.; Scott, A. M.; Klein, O.; Ernst, M. Enhancing therapeutic anti-cancer responses by combining immune checkpoint and tyrosine kinase inhibition. *Molecular cancer* **2022**, *21* (1), 189.
(24) Wang, Y.; Zhao, Q.; Zhao, B.; Zheng, Y.; Zhuang, Q.; Liao, N.; Wang, P.; Cai, Z.; Zhang, D.; Zeng, Y.; Liu, X. Remodeling Tumor-Associated Neutrophils to Enhance Dendritic Cell-Based HCC Neoantigen Nano-Vaccine Efficiency. *Advanced science (Weinheim, Baden-Wurttemberg, Germany)* **2022**, *9* (11), No. e2105631.
(25) Kobayashi, H.; Enomoto, A.; Woods, S. L.; Burt, A. D.; Takahashi, M.; Worthley, D. L. Cancer-associated fibroblasts in gastrointestinal cancer. *Nature reviews. Gastroenterology & hepatology* **2019**, *16* (5), 282−295.
(26) Binnewies, M.; Roberts, E. W.; Kersten, K.; Chan, V.; Fearon, D. F.; Merad, M.; Coussens, L. M.; Gabrilovich, D. I.; Ostrand-Rosenberg, S.; Hedrick, C. C.; Vonderheide, R. H.; Pittet, M. J.; Jain, R. K.; Zou, W.; Howcroft, T. K.; Woodhouse, E. C.; Weinberg, R. A.; Krummel, M. F. Understanding the tumor immune microenvironment (TIME) for effective therapy. *Nature medicine* **2018**, *24* (5), 541−550.
(27) Guo, J.; Zeng, H.; Shi, X.; Han, T.; Liu, Y.; Liu, Y.; Liu, C.; Qu, D.; Chen, Y. A CFH peptide-decorated liposomal oxymatrine inactivates cancer-associated fibroblasts of hepatocellular carcinoma through epithelial-mesenchymal transition reversion. *J. Nanobiotechnol.* **2022**, *20* (1), 114.
(28) Yu, Y. R.; Imrichova, H.; Wang, H.; Chao, T.; Xiao, Z.; Gao, M.; Rincon-Restrepo, M.; Franco, F.; Genolet, R.; Cheng, W. C.; Jandus, C.; Coukos, G.; Jiang, Y. F.; Locasale, J. W.; Zippelius, A.; Liu, P. S.; Tang, L.; Bock, C.; Vannini, N.; Ho, P. C. Disturbed mitochondrial dynamics in CD8(+) TILs reinforce T cell exhaustion. *Nature immunology* **2020**, *21* (12), 1540−1551.
(29) Scharping, N. E.; Menk, A. V.; Moreci, R. S.; Whetstone, R. D.; Dadey, R. E.; Watkins, S. C.; Ferris, R. L.; Delgoffe, G. M. The Tumor Microenvironment Represses T Cell Mitochondrial Biogenesis to Drive Intratumoral T Cell Metabolic Insufficiency and Dysfunction. *Immunity* **2016**, *45* (2), 374−88.
(30) Al-Habsi, M.; Chamoto, K.; Matsumoto, K.; Nomura, N.; Zhang, B.; Sugiura, Y.; Sonomura, K.; Maharani, A.; Nakajima, Y.; Wu, Y.; Nomura, Y.; Menzies, R.; Tajima, M.; Kitaoka, K.; Haku, Y.; Delghandi, S.; Yurimoto, K.; Matsuda, F.; Iwata, S.; Ogura, T.; Fagarasan, S.; Honjo, T. Spermidine activates mitochondrial trifunctional protein and improves antitumor immunity in mice. *Science (New York, N.Y.)* **2022**, *378* (6618), No. eabj3510.
(31) Jiang, B.; Yang, Y. J.; Dang, W. Z.; Li, H.; Feng, G. Z.; Yu, X. C.; Shen, X. Y.; Hu, X. G. Astragaloside IV reverses simvastatin-induced skeletal muscle injury by activating the AMPK-PGC-1α signalling pathway. *Phytotherapy research: PTR* **2020**, *34* (5), 1175−1184.
(32) Xia, Q.; Wang, H.; Huang, B.; Yuan, X.; Zhang, J.; Zhang, J.; Jiang, L.; Xiong, T.; Zeng, G. State-of-the-Art Advances and Challenges of Iron-Based Metal Organic Frameworks from Attractive Features, Synthesis to Multifunctional Applications. *Small (Weinheim an der Bergstrasse, Germany)* **2019**, *15* (2), No. e1803088.
(33) Bindra, A. K.; Wang, D.; Zhao, Y. Metal-Organic Frameworks Meet Polymers: From Synthesis Strategies to Healthcare Applications. *Advanced materials (Deerfield Beach, Fla.)* **2023**, *35*, No. e2300700.
(34) Liu, J.; Huang, J.; Zhang, L.; Lei, J. Multifunctional metal-organic framework heterostructures for enhanced cancer therapy. *Chem. Soc. Rev.* **2021**, *50* (2), 1188−1218.
(35) Illes, B.; Wuttke, S.; Engelke, H. Liposome-Coated Iron Fumarate Metal-Organic Framework Nanoparticles for Combination Therapy. *Nanomaterials (Basel, Switzerland)* **2017**, *7* (11), 351.
(36) Yang, J.; Ma, S.; Xu, R.; Wei, Y.; Zhang, J.; Zuo, T.; Wang, Z.; Deng, H.; Yang, N.; Shen, Q. Smart biomimetic metal organic frameworks based on ROS-ferroptosis-glycolysis regulation for enhanced tumor chemo-immunotherapy. *Journal of controlled release: official journal of the Controlled Release Society* **2021**, *334*, 21−33.
(37) Wu, M. X.; Yang, Y. W. Metal-Organic Framework (MOF)-Based Drug/Cargo Delivery and Cancer Therapy. *Advanced materials (Deerfield Beach, Fla.)* **2017**, *29* (23). DOI: 10.1002/adma.201606134
(38) Yang, Y.; Xia, F.; Yang, Y.; Gong, B.; Xie, A.; Shen, Y.; Zhu, M. Litchi-like Fe(3)O(4)@Fe-MOF capped with HAp gatekeepers for pH-triggered drug release and anticancer effect. *Journal of materials chemistry. B* **2017**, *5* (43), 8600−8606.
(39) Li, D.; Xiong, W.; Wang, Y.; Feng, J.; He, Y.; Du, J.; Wang, J.; Yang, M.; Zeng, H.; Yang, Y. G.; Wu, N.; Chen, S.; Dong, Z. SLAMF3 and SLAMF4 are immune checkpoints that constrain macrophage phagocytosis of hematopoietic tumors. *Science immunology* **2022**, *7* (67), No. eabj5501.
(40) Jeanne, A.; Sarazin, T.; Charlé, M.; Kawecki, C.; Kauskot, A.; Hedtke, T.; Schmelzer, C. E. H.; Martiny, L.; Maurice, P.; Dedieu, S. Towards the Therapeutic Use of Thrombospondin 1/CD47 Targeting TAX2 Peptide as an Antithrombotic Agent. *Arterioscler., Thromb., Vasc. Biol.* **2020**, *41* (1), No. e1-e17.
(41) Zou, J.; He, J.; Wang, X.; Wang, Y.; Wu, C.; Shi, M.; Jiang, H.; Wu, Z.; Liu, J.; Zhang, W. Glycoprotein Ib-regulated micro platelet ghost for biosafe distribution and photothermal oncotherapy. *Journal of controlled release: official journal of the Controlled Release Society* **2022**, *351*, 341−360.

https://doi.org/10.1021/acsnano.3c07885
ACS Nano 2023, 17, 23829−23849

(42) Lin, L.; Hu, Y.; Guo, Z.; Chen, J.; Sun, P.; Tian, H.; Chen, X. Gene-guided OX40L anchoring to tumor cells for synergetic tumor "self-killing" immunotherapy. *Bioactive materials* **2023**, *25*, 689−700.
(43) Yin, N.; Wang, Y.; Liu, Y.; Niu, R.; Zhang, S.; Cao, Y.; Lv, Z.; Song, S.; Liu, X.; Zhang, H. A Cholesterol Metabolic Regulated Hydrogen-Bonded Organic Framework (HOF)-based Biotuner for Antibody Non-dependent Immunotherapy Tailored for Glioblastoma. *Advanced materials (Deerfield Beach, Fla.)* **2023**, *35*, No. e2303567.
(44) Zhang, B.; Zhang, J.; Li, Y.; Li, N.; Wang, Y.; Jang, R.; Xu, X.; Li, R.; Chen, Z.; Duan, S.; Wang, Y.; Zhang, L. In Situ STING-Activating Nanovaccination with TIGIT Blockade for Enhanced Immunotherapy of Anti-PD-1-Resistant Tumors. *Advanced materials (Deerfield Beach, Fla.)* **2023**, *35* (24), No. e2300171.
(45) Caligiuri, G.; Tuveson, D. A. Activated fibroblasts in cancer: Perspectives and challenges. *Cancer cell* **2023**, *41* (3), 434−449.
(46) Hulse, K. E.; Reefer, A. J.; Engelhard, V. H.; Satinover, S. M.; Patrie, J. T.; Chapman, M. D.; Woodfolk, J. A. Targeting Fel d 1 to FcgammaRI induces a novel variation of the T(H) 2 response in subjects with cat allergy. *Journal of allergy and clinical immunology* **2008**, *121* (3), 756−762.e4.
(47) Mazzocca, A.; Dituri, F.; Lupo, L.; Quaranta, M.; Antonaci, S.; Giannelli, G. Tumor-secreted lysophostatidic acid accelerates hepatocellular carcinoma progression by promoting differentiation of peritumoral fibroblasts in myofibroblasts. *Hepatology (Baltimore, Md.)* **2011**, *54* (3), 920−30.
(48) Shao, M.; Ning, F.; Zhao, J.; Wei, M.; Evans, D. G.; Duan, X. Preparation of Fe3O4@SiO2@layered double hydroxide core-shell microspheres for magnetic separation of proteins. *J. Am. Chem. Soc.* **2012**, *134* (2), 1071−7.
(49) Senosy, I. A.; Zhang, X. Z.; Lu, Z. H.; Guan, X. Y.; Yang, Z. H.; Li, J. H.; Guo, H. M.; Abdelrahman, T. M.; Mmby, M.; Gbiliy, A. Magnetic metal-organic framework MIL-100 (Fe)/polyethyleneimine composite as an adsorbent for the magnetic solid-phase extraction of fungicides and their determination using HPLC-UV. *Mikrochimica acta* **2021**, *188* (2), 33.
(50) Jian, X.; Xu, J.; Yang, L.; Zhao, C.; Xu, J.; Gao, Z.; Song, Y. Y. Intracellular Metal-Organic Frameworks: Integrating an All-In-One Semiconductor Electrode Chip for Therapy, Capture, and Quantification of Circulating Tumor Cells. *Analytical chemistry* **2020**, *92* (19), 13319−13326.
(51) Aslam, S.; Zeng, J.; Subhan, F.; Li, M.; Lyu, F.; Li, Y.; Yan, Z. In situ one-step synthesis of Fe(3)O(4)@MIL-100(Fe) core-shells for adsorption of methylene blue from water. *J. Colloid Interface Sci.* **2017**, *505*, 186−195.
(52) Du, X.; Zhang, Z.; Zheng, X.; Zhang, H.; Dong, D.; Zhang, Z.; Liu, M.; Zhou, J. An electrochemical biosensor for the detection of epithelial-mesenchymal transition. *Nat. Commun.* **2020**, *11* (1), 192.
(53) Oroojalian, F.; Beygi, M.; Baradaran, B.; Mokhtarzadeh, A.; Shahbazi, M. A. Immune Cell Membrane-Coated Biomimetic Nanoparticles for Targeted Cancer Therapy. *Small (Weinheim an der Bergstrasse, Germany)* **2021**, *17* (12), No. e2006484.
(54) Hu, C. M.; Fang, R. H.; Wang, K. C.; Luk, B. T.; Thamphiwatana, S.; Dehaini, D.; Nguyen, P.; Angsantikul, P.; Wen, C. H.; Kroll, A. V.; Carpenter, C.; Ramesh, M.; Qu, V.; Patel, S. H.; Zhu, J.; Shi, W.; Hofman, F. M.; Chen, T. C.; Gao, W.; Zhang, K.; Chien, S.; Zhang, L. Nanoparticle biointerfacing by platelet membrane cloaking. *Nature* **2015**, *526* (7571), 118−21.
(55) Wang, D.; Zhou, J.; Chen, R.; Shi, R.; Xia, G.; Zhou, S.; Liu, Z.; Zhang, N.; Wang, H.; Guo, Z.; Chen, Q. Magnetically guided delivery of DHA and Fe ions for enhanced cancer therapy based on pH-responsive degradation of DHA-loaded Fe3O4@C@MIL-100(Fe) nanoparticles. *Biomaterials* **2016**, *107*, 88−101.
(56) Chen, X.; Zhang, Y.; Zhao, Y.; Wang, S.; Liu, L.; Xu, W.; Guo, Z.; Wang, S.; Liu, Y.; Zhang, J. Encapsulating Pt Nanoparticles through Transforming Fe(3)O(4) into MIL-100(Fe) for Well-Defined Fe(3)O(4)@Pt@MIL-100(Fe) Core-Shell Heterostructures with Promoting Catalytic Activity. *Inorganic chemistry* **2019**, *58* (18), 12433−12440.
(57) Cun, J. E.; Pan, Y.; Zhang, Z.; Lu, Y.; Li, J.; Pan, Q.; Gao, W.; Luo, K.; He, B.; Pu, Y. Photo-enhanced upcycling H(2)O(2) into hydroxyl radicals by IR780-embedded Fe(3)O(4)@MIL-100 for intense nanocatalytic tumor therapy. *Biomaterials* **2022**, *287*, 121687.
(58) Fenaroli, F.; Westmoreland, D.; Benjaminsen, J.; Kolstad, T.; Skjeldal, F. M.; Meijer, A. H.; van der Vaart, M.; Ulanova, L.; Roos, N.; Nyström, B.; Hildahl, J.; Griffiths, G. Nanoparticles as drug delivery system against tuberculosis in zebrafish embryos: direct visualization and treatment. *ACS Nano* **2014**, *8* (7), 7014−26.
(59) Yang, W.; Frickenstein, A. N.; Sheth, V.; Holden, A.; Mettenbrink, E. M.; Wang, L.; Woodward, A. A.; Joo, B. S.; Butterfield, S. K.; Donahue, N. D.; Green, D. E.; Thomas, A. G.; Harcourt, T.; Young, H.; Tang, M.; Malik, Z. A.; Harrison, R. G.; Mukherjee, P.; DeAngelis, P. L.; Wilhelm, S. Controlling Nanoparticle Uptake in Innate Immune Cells with Heparosan Polysaccharides. *Nano Lett.* **2022**, *22* (17), 7119−7128.
(60) Olsson, M.; Bruhns, P.; Frazier, W. A.; Ravetch, J. V.; Oldenborg, P. A. Platelet homeostasis is regulated by platelet expression of CD47 under normal conditions and in passive immune thrombocytopenia. *Blood* **2005**, *105* (9), 3577−82.
(61) Zhang, K.; Wang, Z. Q.; Liu, Z.; Qu, T.; Zhang, Z.; Zeng, F.; Song, H.; Shi, Q.; Kang, Z.; Chen, B.; Dai, P.; Guo, P.; Tong, Z.; Xu, W. A Self-Disguised Nanospy for Improving Drug Delivery Efficiency *via* Decreasing Drug Protonation. *Small (Weinheim an der Bergstrasse, Germany)* **2023**, *19* (25), No. e2300060.
(62) Belhadj, Z.; He, B.; Deng, H.; Song, S.; Zhang, H.; Wang, X.; Dai, W.; Zhang, Q. A combined "eat me/don't eat me" strategy based on extracellular vesicles for anticancer nanomedicine. *Journal of extracellular vesicles* **2020**, *9* (1), 1806444.
(63) Filliol, A.; Saito, Y.; Nair, A.; Dapito, D. H.; Yu, L. X.; Ravichandra, A.; Bhattacharjee, S.; Affo, S.; Fujiwara, N.; Su, H.; Sun, Q.; Savage, T. M.; Wilson-Kanamori, J. R.; Caviglia, J. M.; Chin, L.; Chen, D.; Wang, X.; Caruso, S.; Kang, J. K.; Amin, A. D.; Wallace, S.; Dobie, R.; Yin, D.; Rodriguez-Fiallos, O. M.; Yin, C.; Mehal, A.; Izar, B.; Friedman, R. A.; Wells, R. G.; Pajvani, U. B.; Hoshida, Y.; Remotti, H. E.; Arpaia, N.; Zucman-Rossi, J.; Karin, M.; Henderson, N. C.; Tabas, I.; Schwabe, R. F. Opposing roles of hepatic stellate cell subpopulations in hepatocarcinogenesis. *Nature* **2022**, *610* (7931), 356−365.
(64) Zhu, A. X.; Chen, D.; He, W.; Kanai, M.; Voi, M.; Chen, L. T.; Daniele, B.; Furuse, J.; Kang, Y. K.; Poon, R. T.; Vogel, A.; Chiang, D. Y. Integrative biomarker analyses indicate etiological variations in hepatocellular carcinoma. *Journal of hepatology* **2016**, *65* (2), 296−304.
(65) Roullet, S.; Luc, N.; Rayes, J.; Solarz, J.; Disharoon, D.; Ditto, A.; Gahagan, E.; Pawlowski, C.; Sefiane, T.; Adam, F.; Casari, C.; Christophe, O. D.; Bruckman, M.; Lenting, P. J.; Sen Gupta, A.; Denis, C. V. Efficacy of platelet-inspired hemostatic nanoparticles on bleeding in von Willebrand disease murine models. *Blood* **2023**, *141* (23), 2891−2900.
(66) Leberzammer, J.; Agten, S. M.; Blanchet, X.; Duan, R.; Ippel, H.; Megens, R. T. A.; Schulz, C.; Aslani, M.; Duchene, J.; Döring, Y.; Jooss, N. J.; Zhang, P.; Brandl, R.; Stark, K.; Siess, W.; Jurk, K.; Heemskerk, J. W. M.; Hackeng, T. M.; Mayo, K. H.; Weber, C.; von Hundelshausen, P. Targeting platelet-derived CXCL12 impedes arterial thrombosis. *Blood* **2022**, *139* (17), 2691−2705.
(67) Verginadis, I. I.; Avgousti, H.; Monslow, J.; Skoufos, G.; Chinga, F.; Kim, K.; Leli, N. M.; Karagounis, I. V.; Bell, B. I.; Velalopoulou, A.; Salinas, C. S.; Wu, V. S.; Li, Y.; Ye, J.; Scott, D. A.; Osterman, A. L.; Sengupta, A.; Weljie, A.; Huang, M.; Zhang, D.; Fan, Y.; Radaelli, E.; Tobias, J. W.; Rambow, F.; Karras, P.; Marine, J. C.; Xu, X.; Hatzigeorgiou, A. G.; Ryeom, S.; Diehl, J. A.; Fuchs, S. Y.; Puré, E.; Koumenis, C. A stromal Integrated Stress Response activates perivascular cancer-associated fibroblasts to drive angiogenesis and tumour progression. *Nature cell biology* **2022**, *24* (6), 940−953.
(68) Hu, C.; Liu, X.; Ran, W.; Meng, J.; Zhai, Y.; Zhang, P.; Yin, Q.; Yu, H.; Zhang, Z.; Li, Y. Regulating cancer associated fibroblasts with losartan-loaded injectable peptide hydrogel to potentiate chemo-

https://doi.org/10.1021/acsnano.3c07885
ACS Nano 2023, 17, 23829−23849

therapy in inhibiting growth and lung metastasis of triple negative breast cancer. *Biomaterials* **2017**, *144*, 60−72.
(69) Sharbeen, G.; McCarroll, J. A.; Akerman, A.; Kopecky, C.; Youkhana, J.; Kokkinos, J.; Holst, J.; Boyer, C.; Erkan, M.; Goldstein, D.; Timpson, P.; Cox, T. R.; Pereira, B. A.; Chitty, J. L.; Fey, S. K.; Najumudeen, A. K.; Campbell, A. D.; Sansom, O. J.; Ignacio, R. M. C.; Naim, S.; Liu, J.; Russia, N.; Lee, J.; Chou, A.; Johns, A.; Gill, A. J.; Gonzales-Aloy, E.; Gebski, V.; Guan, Y. F.; Pajic, M.; Turner, N.; Apte, M. V.; Davis, T. P.; Morton, J. P.; Haghighi, K. S.; Kasparian, J.; McLean, B. J.; Setargew, Y. F.; Phillips, P. A. Cancer-Associated Fibroblasts in Pancreatic Ductal Adenocarcinoma Determine Response to SLC7A11 Inhibition. *Cancer research* **2021**, *81* (13), 3461−3479.
(70) Ding, B. W.; Liu, Y. J. Bioluminescence of Firefly Squid *via* Mechanism of Single Electron-Transfer Oxygenation and Charge-Transfer-Induced Luminescence. *J. Am. Chem. Soc.* **2017**, *139* (3), 1106−1119.
(71) Llovet, J. M.; Lencioni, R. mRECIST for HCC: Performance and novel refinements. *Journal of hepatology* **2020**, *72* (2), 288−306.
(72) Innes, H.; Nahon, P. Statistical perspectives on using hepatocellular carcinoma risk models to inform surveillance decisions. *Journal of hepatology* **2023**, *79*, 1332−1337.
(73) Kim, J.; DeBerardinis, R. J. Mechanisms and Implications of Metabolic Heterogeneity in Cancer. *Cell metabolism* **2019**, *30* (3), 434−446.
(74) Scharping, N. E.; Rivadeneira, D. B.; Menk, A. V.; Vignali, P. D. A.; Ford, B. R.; Rittenhouse, N. L.; Peralta, R.; Wang, Y.; Wang, Y.; DePeaux, K.; Poholek, A. C.; Delgoffe, G. M. Mitochondrial stress induced by continuous stimulation under hypoxia rapidly drives T cell exhaustion. *Nature immunology* **2021**, *22* (2), 205−215.
(75) Lee, C. C.; Stiebritz, M. T.; Hu, Y. Reactivity of [Fe(4)S(4)] Clusters toward C1 Substrates: Mechanism, Implications, and Potential Applications. *Accounts of chemical research* **2019**, *52* (5), 1168−1176.
(76) Zhu, M.; Min, S.; Mao, X.; Zhou, Y.; Zhang, Y.; Li, W.; Li, L.; Wu, L.; Cong, X.; Yu, G. Interleukin-13 promotes cellular senescence through inducing mitochondrial dysfunction in IgG4-related sialadenitis. *International journal of oral science* **2022**, *14* (1), 29.
(77) Chen, S. W.; Zhu, S. Q.; Pei, X.; Qiu, B. Q.; Xiong, D.; Long, X.; Lin, K.; Lu, F.; Xu, J. J.; Wu, Y. B. Cancer cell-derived exosomal circUSP7 induces CD8(+) T cell dysfunction and anti-PD1 resistance by regulating the miR-934/SHP2 axis in NSCLC. *Molecular cancer* **2021**, *20* (1), 144.
(78) Shi, L.; Lu, J.; Zhong, D.; Song, M.; Liu, J.; You, W.; Li, W. H.; Lin, L.; Shi, D.; Chen, Y. Clinicopathological and predictive value of MAIT cells in non-small cell lung cancer for immunotherapy. *Journal for immunotherapy of cancer* **2023**, *11* (1), No. e005902.
(79) Intlekofer, A. M.; Takemoto, N.; Wherry, E. J.; Longworth, S. A.; Northrup, J. T.; Palanivel, V. R.; Mullen, A. C.; Gasink, C. R.; Kaech, S. M.; Miller, J. D.; Gapin, L.; Ryan, K.; Russ, A. P.; Lindsten, T.; Orange, J. S.; Goldrath, A. W.; Ahmed, R.; Reiner, S. L. Effector and memory CD8+ T cell fate coupled by T-bet and eomesodermin. *Nature immunology* **2005**, *6* (12), 1236−44.
(80) Liu, Z.; Zhao, L.; Liu, H.; Dong, N.; Zhou, N.; Zhang, Y.; Yin, T.; He, H.; Gou, J.; Tang, X.; Yang, L.; Gao, S. Norcantharidin liposome emulsion hybrid delivery system enhances PD-1/PD-L1 immunotherapy by agonizing the non-canonical NF-κB pathway. *International journal of pharmaceutics* **2022**, *628*, 122361.

https://doi.org/10.1021/acsnano.3c07885
ACS Nano 2023, 17, 23829−23849